Estimating the Mass of UO$_3$ Powder in a Container Using MCNP-PoliMi Simulations of NMIS Measurements

An Engineering Project
Presented for the
Master of Science
Degree
The University of Tennessee, Knoxville

Brandon R. Grogan
January 2008

REPORT OF FINAL EXAMINATION/ DEFENSE OF THESIS
MASTER'S OR SPECIALIST IN EDUCATION DEGREES

The University of Tennessee
The Graduate School

This is to certify that

_____
(student name)

a candidate for the _____ degree,

_____
(passed or failed)

the final examination in partial fulfillment of the requirements.

Date: _____

Student ID #: _____

Committee Names and Signatures

_____
Name (Chairperson)   Signature

_____
Name   Signature

_____
Name   Signature

_____
Name   Signature

_____
Name   Signature

Submit Exam Results by Deadline to:
The Graduate School
P-105 Andy Holt Tower
Knoxville, TN 37996-0104

ACKNOWLEDGEMENTS

ABSTRACT

The Nuclear Materials Identification System (NMIS) uses fast neutrons to conduct non-intrusive scans of both fissile and non-fissile materials. By time-tagging the source neutrons, the NMIS processor can measure the time of flight of these neutrons through the target of the scan and into detectors on the opposite side. With a monoenergetic neutron source, such as a DT generator, these time-of-flight measurements can approximately determine the number of neutrons that travel through the target uncollided. By comparing the results of a scan on an empty container and one made on a container with unknown materials inside, the NMIS processor can subtract the container and determine the configuration of materials inside.

Using multiple small detectors, and many horizontal and vertical samples, the NMIS system can produce a picture of the object being scanned, known as a neutron radiograph. With this radiograph, it is thought that other characteristics of the scanned material can be inferred. In this thesis, the material being scanned consists of highly enriched uranium trioxide (UO_3) powder. Using the results of the time-of-flight measurements from two reference scans, a container with an unknown configuration was scanned and the mass of the UO_3 powder inside was estimated. The MCNP-PoliMi computer code was used to simulate these scans. The process was applied to three different unknown geometries of powder, and the scan of each geometry was simulated using three different measurement times, resulting in a total of nine simulated scans.

All of the simulated scans produced a mass estimate that is within 3% of the true mass inside of the container. An analysis of the uncertainty in these measurements determined that the error in the estimates is much larger than the uncertainty in most cases, indicating that the algorithm used to determine the mass produces some systematic error in the results. For powder configurations which are fairly close to those modeled here, this systematic error should be small enough to neglect, but for substantially different models, a correction to the algorithm may be required.

TABLE OF CONTENTS

LIST OF TABLES

LIST OF FIGURES

LIST OF ABBREVIATIONS

μA	microamp
ASCII	American Standard Code for Information Interchange
BC	Bicron
CAD	computer aided design
CAT	catalog
cm	centimeter
cps	counts per second
DAUI	Data Acquisition User Interface
DT	deuterium tritium
EJ	Eljen
G	gram
GHz	gigahertz
HEU	highly enriched uranium
IDAS	Interactive Data Analysis System
keV	kilo electron Volts
kg	kilogram
kV	kilovolts
MCNP	Monte Carlo N-Particle
MeV	mega electron volt
mm	millimeter
mol	mole
NMD	Nuclear Material Data
NMIS	Nuclear Materials Identification
Ns	nanosecond
PMT	photomultiplier tube
PoliMi	Politecnico di Milano
RAM	random access memory
UO^3	uranium trioxide

1. Introduction

The Nuclear Materials Identification System (NMIS) was developed at the Oak Ridge National Laboratory and at the Y-12 National Security Complex for the purposes of characterizing both fissile and non-fissile material. [1] The NMIS uses active neutron interrogation to conduct non-intrusive scans of objects inside sealed containers. In the past, the NMIS has been used to image objects that could not be readily accessed and physically inspected. [2, 3]

The NMIS consists of three components: a neutron source, two or more fast detectors, and computer hardware and software that measure time correlations between the detectors to ~1-ns accuracy. [4] By time-tagging the source neutrons, the NMIS can then measure the time of flight of the neutrons through the target to detectors on the opposite side. If the neutron source is monoenergetic, this time of flight measurement can then be used to measure the number of neutrons which pass through the target uncollided. By measuring an empty container and then one with unknown contents, the effective attenuation of the contents of the container can be determined.

For the purpose of this paper, the goal is to determine if, given a known isotopic makeup of the material inside of a container, the NMIS system can successfully determine the mass of the contents. The contents will be uranium trioxide (UO_3) powder with an unknown mass and density profile. The Monte-Carlo N-Particle - Politecnico di Milano computer code will be used to simulate the NMIS scans, and custom algorithms will be derived in order to estimate the mass of the various simulated measurements of the unknowns.

2. Nuclear Materials Identification System

2.1 DT Generator

In the modeled configuration, a deuterium-tritium (DT) generator is used for the neutron source. The DT generator produces neutrons using the reaction [5]:

$$^{3}H + {^{2}H} \rightarrow {^{4}He} + n + 17.6 MeV .$$ (1)

Because the reaction results in only two products, each will have a unique energy determined by their relative masses. In the center-of-mass coordinate system, the resulting neutron has an energy of:

$$E_n = \frac{m_\alpha}{m_\alpha + m_n} Q \cong \frac{4}{5} \times 17.6 MeV = 14.1 \, \text{MeV}.$$ (2)

In the laboratory coordinate system, the initial kinetic energy of the deuteron or triton will cause anisotropy in the neutron energies, with neutrons traveling in the same direction as the deuteron or triton having the greatest energy and those traveling in the opposite direction having the least. However, since the particles are accelerated with a relatively low 70-90kV voltage [6], their energies are small compared to 14.1 MeV, and the neutrons can be treated as effectively

monoenergetic in the laboratory coordinate system. Using relativistic kinematics, the velocity of a 14.1 MeV neutron can be found using the equation:

$$\beta = \frac{v}{c} = \sqrt{1 - \frac{1}{\frac{E_n}{m_n c^2}}} \Rightarrow v = c \cdot \sqrt{1 - \frac{1}{\frac{T_n + m_n c^2}{m_n c^2}}} \tag{3}$$

where v is the neutron speed, c is the speed of light in a vacuum, T_n is the neutron kinetic energy, E_n is the neutron total energy, and m_n is the neutron rest mass. The speed of light in a vacuum is 3.00×10^8 m/s, or 30.0 cm/ns. At 14.1 MeV, a neutron has a speed of 0.17c, which equals 5.1 cm/ns.

The neutron and alpha particle products will travel away from the reaction site back-to-back. Because of their charge and mass, alpha particles can be detected with a very thin detector. If an alpha detector is placed on one side of the DT target, then pulses in the alpha detector will correspond to neutrons traveling in the opposite direction. [7]
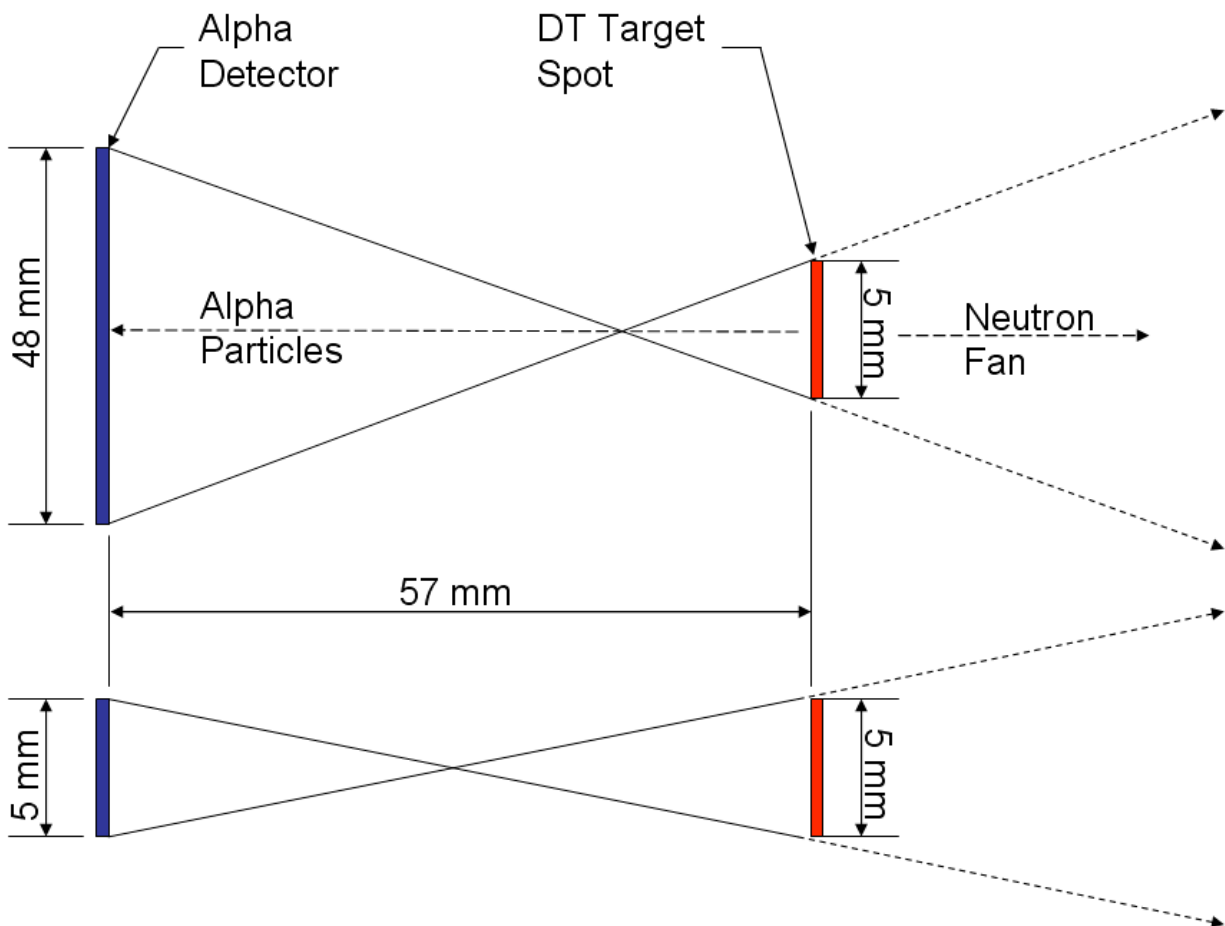
Figure 1　　　**The geometry of the DT generator target spot and alpha detector**

Figure 1 shows approximate the geometry of the DT target (where the actual DT reaction occurs) and the alpha detector utilized in the NMIS. The top image is the horizontal profile and the bottom one is the vertical profile. The corresponding half-angles of the fans are then:

$$\theta_{1/2} = \tan^{-1}\left(\frac{\frac{1}{2}\ell_\alpha + \frac{1}{2}\ell_{ts}}{D}\right), \tag{4}$$

where ℓ_α and ℓ_{ts} are the dimensions of the alpha detector and DT target spot, respectively, and D is the distance between them. This geometry results in a fan with a horizontal half-angle of 24.9° and a vertical half-angle of 5.0°. The rate of neutron production depends on the model used, as well as the high-voltage and target current settings of the particular DT generator. The model normally used with the NMIS is an API-120 DT generator manufactured by the Thermo Electron Corporation. Nominally, this generator produces on the order of 10^7 neutrons per second produced isotropically. For the purposes of this paper, the source strength will be assumed to be 3×10^7 neutrons per second, which approximately corresponds to the neutron output produced by an API-120 operating at 90kV tube voltage and 50μA beam current.

2.2 Detectors

The fan of neutrons defined by the DT generator is aimed toward the target of interest, and the detectors are placed on the opposite side of the target. In the modeled configuration, the NMIS uses an array of 24 fast plastic scintillators. These detectors use BC-420 (EJ-230) crystals with dimensions of 1" × 1" × 6" (2.54 × 2.54 × 15.24 cm). This material produces ultra fast timing with a decay time of only 1.5 ns. [8] The detectors also feature an integrated photomultiplier tube (PMT) and voltage divider.

Plastic scintillators are sensitive to both neutrons and gamma rays. Because NMIS scans are often conducted in areas with a high background radiation level. A particular nuisance is the 186 keV gamma ray produced from the decay of ^{235}U. In order to eliminate this particular source of background radiation, the detector thresholds are set to approximately one-third of the Compton edge of ^{137}Cs gamma rays. The energy of the Compton edge is given by:

$$E_{CE} = E_\gamma \frac{2E_\gamma}{m_e c^2 + 2E_\gamma}, \tag{5}$$

where E_{CE} is the energy of the Compton edge, E_γ is the initial gamma ray energy, and m_e is the rest mass of an electron. For a 667 keV gamma ray from Cs, the Compton edge is 482 keV and for the 186 keV gamma from ^{235}U it is 78 keV. One-third of the ^{137}Cs Compton edge is 161 keV, which is well above the Compton edge of the 186 keV gamma ray. This threshold energy corresponds to an energy cutoff of approximately 1 MeV for neutrons.

The detectors are mounted on a custom-built detector arm so that their front faces are equidistant from the target spot of the DT generator. A radius of 156 cm is sufficient to allow ~48 detectors

to fit in a horizontal angle of ~45°, which is approximately the extent of the DT Generator's neutron fan. In order to reduce the possible cross-talk between detectors, one empty space (equivalent in size to a detector) was left between each pair of detectors. Thus the arm contains a total of 48 detector positions, of which 24 hold detectors and 24 are empty.

2.3 Hardware

Both the DT neutron generator and the detector arm are mounted on a C-shaped scanner arm. Mechanical actuators produce vertical and angular movement of the scanner arm. For vertical motion, the entire assembly is moved up and down. By taking samples at different heights, the NMIS can combine several horizontal 'slices' of the object being scanned in order to produce an image of the entire object. For angular movement, a second actuator adjusts the position of the detector array relative to the horizontal centerline of the DT fan beam. Because the detector array has an empty space between detectors, it will use this angular motion to move the detectors into the empty spaces in order to see all possible detector angles. For a given 'slice', a scan will first be conducted with all of the detectors at -½ detector (-0.47°) relative to the DT centerline. The detector array will then be shifted over one full detector width to +½ detector (+0.47°) relative to the DT centerline and scanned again. Figure 2 shows a CAD drawing of the scanner arm and associated hardware.
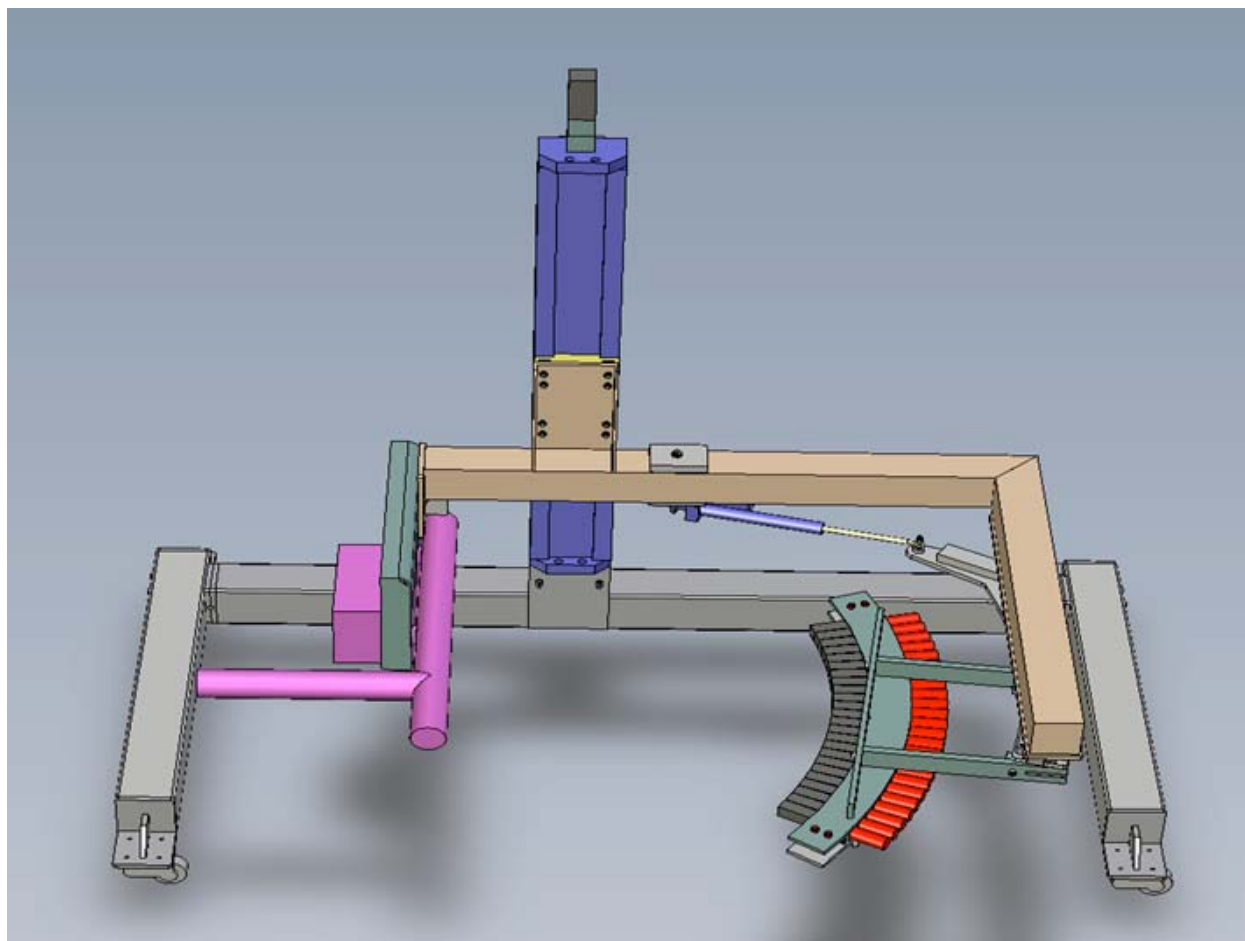
Figure 2   **The NMIS scanner assembly with detectors and DT generator [9]**

The signals from the plastic scintillators are first sent to mixer boxes. Each mixer box combines three detector signals. The mixer boxes use constant fraction discrimination to avoid signal walk. In the output, the mixer box assigns a unique pulse width and delay to each detector so that the NMIS software can ultimately distinguish which detector is pulsing.

The mixer box signals are then sent into a patch panel that is connected to a pair of proprietary NMIS processor boards developed at ORNL. The NMIS processor boards are located in a rack-mounted, Windows XP based personal computer. Each board has five input channels and operates at a 1-GHz synchronous sampling rate. The signal from the alpha detector is fed through a rack-mounted constant fraction discriminator, whose output is split in two. This output is then fed into each of the NMIS processor boards to keep the timing of the two boards in sysc. The equipment rack also contains the power supplies for the scintillators and the alpha detector, as well as other testing equipment used with the NMIS system.

2.4 Software

The NMIS system utilizes two pieces of proprietary ORNL software. The first is the Data Acquisition User Interface (DAUI). The DAUI software allows the user to specify the scan geometry, detector signals, and the number of vertical and angular measurements to include in the scan. The user also controls the measurement time by setting the window size, blocks per loop, and number of loops. The measurement time per sample is then:

$$t_{sample} = n_{loops} \cdot ws \cdot bpl \tag{6}$$

where $\mathbf{n_{loops}}$ is the number of loops, $\mathbf{ws}$ is the window size, and $\mathbf{bpl}$ is the number of blocks per loop. The default window size is 512 ns, and typically 10^7 or 10^8 blocks are collected per loop. This corresponds to a measurement time of 5.12 or 51.2 seconds, which can then be multiplied by any number of loops that are desired. Once the parameters have been entered, the DAUI software can automatically move the mechanical actuators on the scanner assembly and conduct the scan using the specified vertical and angular samples. For each measurement, DAUI writes the measured correlations between each input source to an NMD (Nuclear Material Data) file, as well as a CAT (Catalog) file which list all of the measurements included in the scan.

Once DAUI has finished with the scan, the Interactive Data Analysis System (IDAS) software can read the DAUI output files and calculate cross-correlations between each pair of input signals. The cross-correlations can be viewed graphically in IDAS. Figure 3 is an example of such a graph, showing the positive cross-correlation between the alpha detector and detector number eight. The IDAS software can also combine the scan of an object with a second scan (CAT file) with no object (a void scan). This data can then be exported into a series of CSV (comma separated variable) files. The data in these CSV files can then be used to construct a radiograph of the scanned object by comparing the neutron transmission rate between the target scan and the void scan. This procedure is described in detail in Section 4.
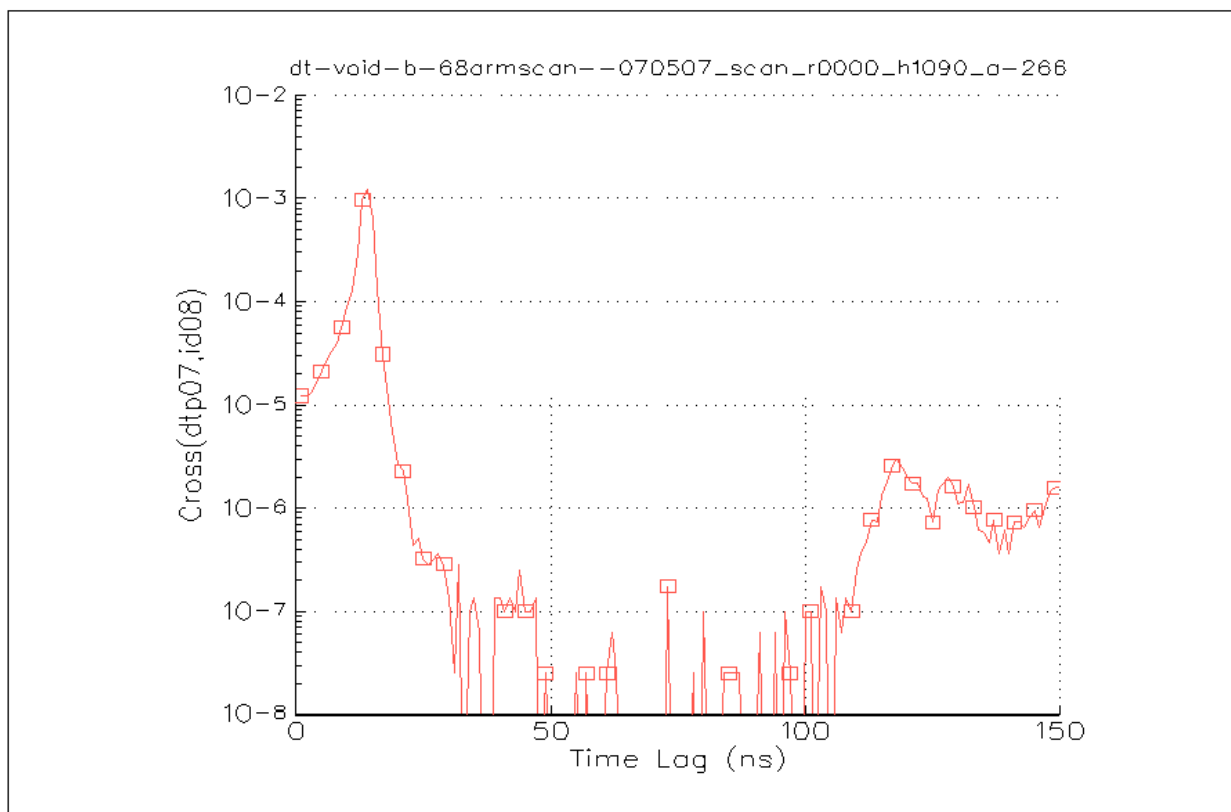
Figure 3   **Time correlation plot between alpha detector and a plastic scintillator**

3. MCNP-PoliMi

In order to simulate a scan by the NMIS system, Monte Carlo methods were used. The Monte Carlo method simulates a large number of identical particles. By applying the Central Limit Theorem, a sample can be used to infer the average behavior of the physical particle population. [10] One of the most popular codes used for this application is the Monte Carlo N-Particle (MCNP) code. While the standard MCNP code generally produces excellent results with regard to the average behavior of the particle population, it often models the physics of a single interaction incorrectly in order to increase efficiency and reduce computing time. [11] Because the time correlation methods used by NMIS correlate detector pulses to individual source particles, the standard version of MCNP is not capable of properly simulating these types of measurements.

The MCNP-PoliMi (Monte Carlo N-Particle-Polytechnic of Milan) code was developed from the standard MCNP-4c code at the University of Milan in Italy. MCNP-PoliMi models each neutron–nucleus interaction as closely to physical reality as possible in order to accurately track each particle for time-of-flight measurements. [12] The MCNP-PoliMi input deck is largely identical to the standard MCNP input deck. It contains a few extra cards which allow the user to specify the detector cells of interest. When executed, MCNP-PoliMi will then generate an ASCII (American Standard Code for Information Interchange) file containing the collision information in the cells of interest. In particular, this information contains the type of particle,

original (source) particle number, location of the collision, target nucleus type, energy imparted by the collision, and the time (after source particle birth) of the collision.

A second program, the MCNP-PoliMi post-processor, is then used to analyze the ASCII file generated by the base MCNP-PoliMi executable. For each collision, the post-processor first determines if the photon or neutron deposited enough energy to overcome the detector threshold and generate a light pulse which would be recorded by the NMIS electronics. If a pulse would be generated, the post-processor then records the collision time in reference to original source event. These correlations are recorded in terms of time bins, which are, by default, 1 ns wide. A separate file is then created for each source-detector correlation consisting of the number of correlations in each time bin.

The MCNP-PoliMi post-processor can also generate detector-detector correlations, and even higher order correlations such as source-detector-detector correlations. However, for the purposes of neutron radiography only the source-detector correlations are required, so they are the only type of correlation measurements that will be examined in this document.

4. Simulation

4.1 Model

The simulations were modeled using the MCNP-PoliMi computer code. Appendix A contains a sample MCNP-PoliMi input deck that was used. The target of the simulation was modeled as a stainless steel trough-shaped container based on a design that might be used to store UO_3 powder. The container walls were 0.95 cm thick and composed of SS-304L stainless steel. The bottom of the container was rounded, with an interior radius of 6.35 cm. Overall, the exterior of the container was 45.7 cm long, 18.9 cm tall, and 14.6 cm wide. Inside of the container is UO_3 powder. The density of the powder can range between 0 g/cm^3 (i.e., a void) and 8 g/cm^3 in any given region of the container depending on the modeled configuration. In all models, the UO_3 powder contained highly enriched uranium (HEU) with a ^{235}U enrichment of 93.15% by weight. Figure 4 shows a diagram of the target.
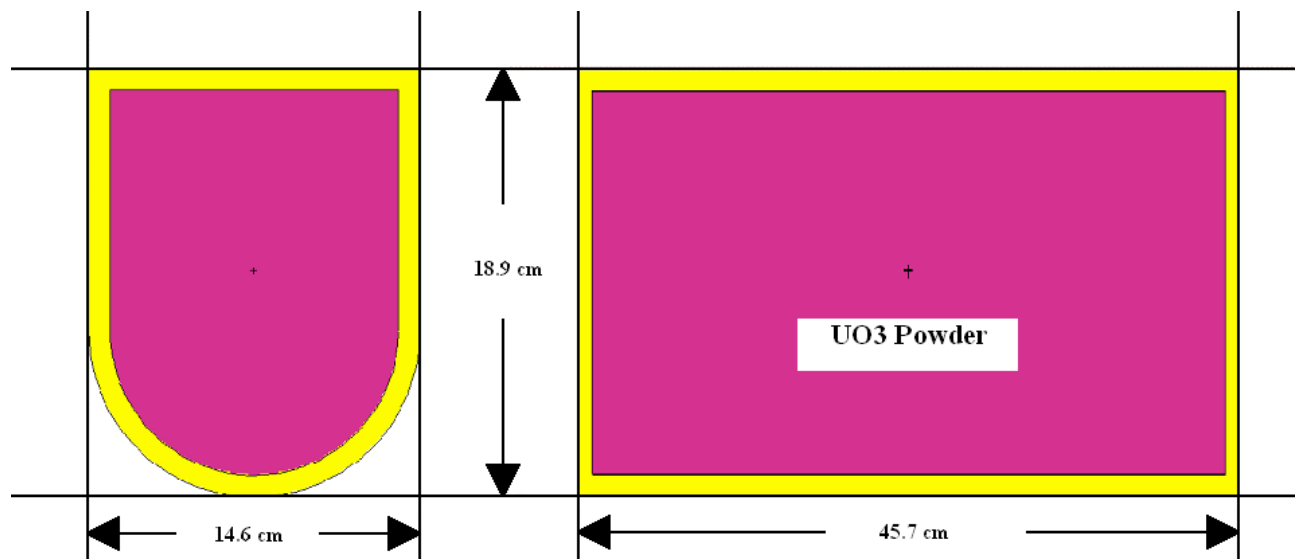
Figure 4   MCNP Diagram of the UO₃ container

The DT generator was modeled as a monoenergetic 14.1-MeV neutron source. The neutrons were generated in a fan 45 degrees wide by 10 degrees high. This is approximately the same as the neutron fan defined by the alpha detector on the physical DT generator, as described in section 2.1. The centerline of the trough was placed 70 cm away from the source and the front faces of the detector array were placed on a circular arc 156 cm away. The 70 cm source to target distance was chosen because it was large enough that the entire trough was contained within the horizontal boundaries of the neutron fan. Similarly, the 156 cm source to detector distance was chosen because at that distance there is room for 48 1" (2.54 cm) detector positions on a 45° circular arc.

24 $1 \times 1 \times 6$ in. $(2.54 \times 2.54 \times 15.24$ cm) fast plastic scintillators were modeled for each simulation and spaced so that there was one open position between each pair of detectors. The detector material was modeled with a $C_{10}H_{11}$ composition and a density of 1.032 g/cm^3. The initial detector positions were assigned so that they were centered on the horizontal center (0°) of the DT neutron fan. Two geometric transforms can then be used to shift the detectors ±½ of the angle subtended by a detector (±0.47°) to simulate two arm angles which covered all 48 detector positions in the DT fan. Similarly, a different transform was used to move the target up and down vertically in order to simulate the measurement of the different horizontal slices which comprise each scan. A diagram of the problem geometry is shown in Figure 5 below.
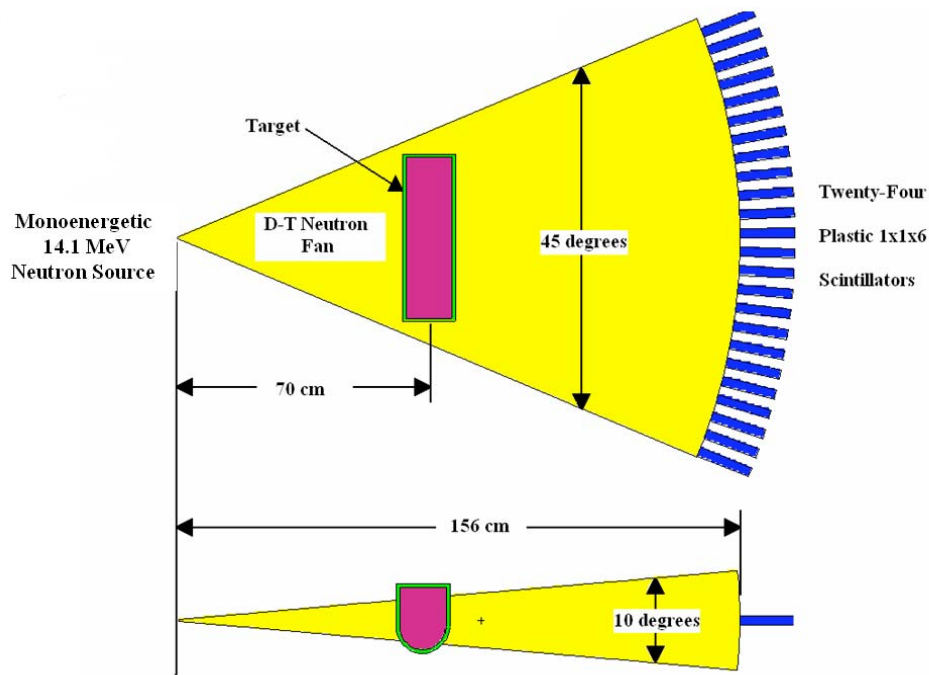
Figure 5   **MCNP-PoliMi problem geometry**

4.2 Simulation Procedure

In order to simulate an NMIS scan, both angular movement of the detector array and combined vertical movement of the DT generator and detectors must be simulated. The angular movement of the detectors was simulated using 2 geometric transforms which placed the 24 detectors at ±½ detector angle (±0.47°) from the horizontal centerline of the DT fan. Similarly, the vertical movement of the DT generator and detectors was simulated by changing the vertical position of the target using another geometric transform. In total, 22 vertical transforms were used, which corresponded to 22 slices of the target spaced 1 cm apart. These slices began with the vertical centerline of the DT fan approximately 1 cm below the lowest point of the container and finished approximately 1 cm above its highest point.

Each sample required its own input deck, so the procedure above required a total of 44 MCNP-PoliMi input decks, 22 vertical slices with 2 arm angles at each slice. In order to accomplish this, two base input decks were written for each simulated scan, representing the two arm angles. A custom FORTRAN-90 code was used to read the base files and produce the 44 individual input decks. A batch file then executed the PoliMi program using each successive input deck, which produced 44 output (DAT) files. A second batch file was then used to run the PoliMi postprocessor on each of the output files. The FORTRAN-90 postprocessor, version 1.8.0, was used. This produced 48 output files, containing the correlation data between the source and each of the 48 detector positions, for each of the 22 slices. In total, each simulated scan produced 48 X 22 = 1056 of these files. Appendix B shows the contents of one of these files.

Each postprocessor output file contains 201 rows and 7 columns of data. The first column is the time after the original source event that the interaction took place. These times represent the 1 ns time bins into which the PoliMi postprocessor divides the correlation data. The second column is the normalized total number of interactions recorded during that time bin. The normalization is performed by dividing the total number of counts recorded during that time bin by the number of source neutrons emitted in the DT fan during the simulated measurement. In MCNP-PoliMi, this value is defined in the 'nps' card. The other columns in these files break the total counts into subcomponents, such as neutrons only or gammas only, which are not used in this paper.

Figure 6 shows the cross-correlation plot produced by graphing the second column (total normalized counts) versus the first column (time lag) from a sample MCNP-PoliMi postprocessor output file. In this example, the target was completely filled with UO_3 powder with a density of 8 g/cm^3. Three distinct features of the time-correlation plot are circled. The first peak results from gamma rays which are created from induced fissions in the uranium nuclei and (n,γ) captures or inelastic scatterings in the steel container. The second, larger, peak consists primarily of 14.1 MeV neutrons that are directly transmitted through the target. The third, much broader, peak consists of neutrons produced by induced fissions and those which suffered multiple scattering reactions. The magnitude of the third peak, relative to the second, increases with increasing enrichment of ^{235}U. In the past, this fact has been used to verify the enrichment of a given configuration of uranium. However, for the purposes of this paper the uranium enrichment is assumed to be a known value and will not deviate from 93.15%.
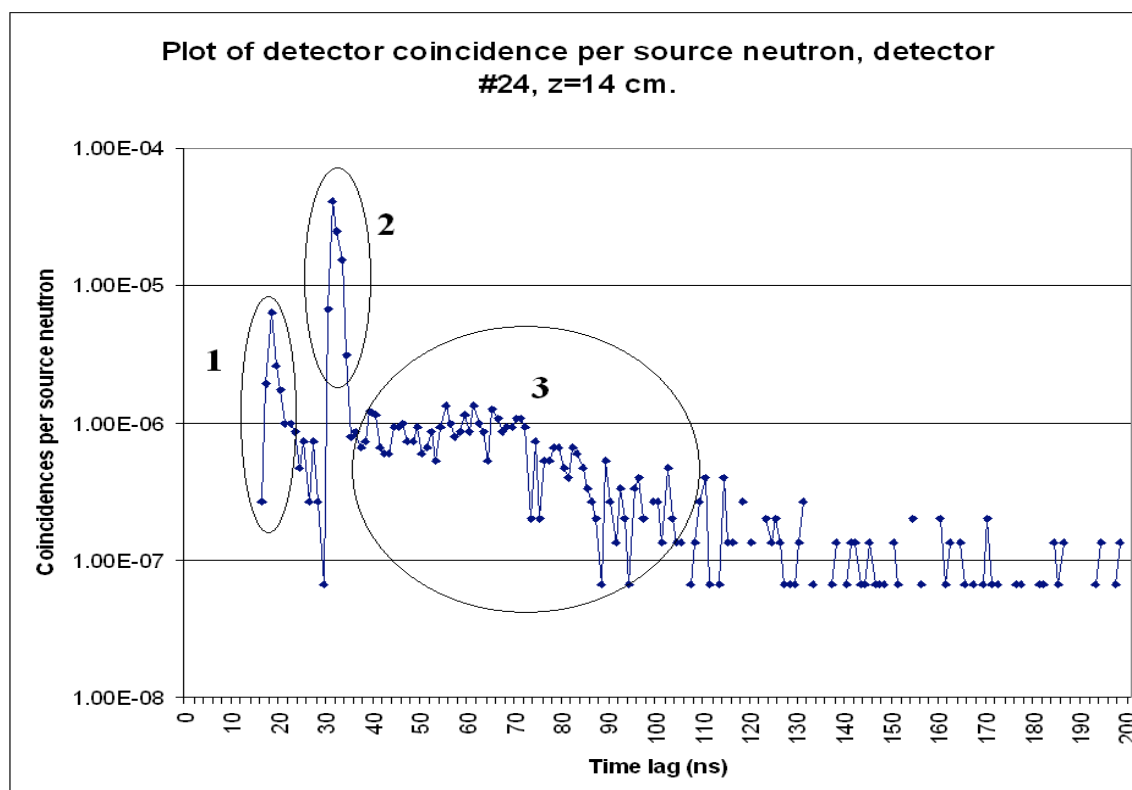
Figure 6   **MCNP-PoliMi cross-correlation between the alpha detector and one of the plastic scintillators in the detector array**

For fast neutron radiography, the desired quantity to measure is the number of neutrons which are directly transmitted through the target. This corresponds to region 2 in Figure 6, above. Nominally, 14.1 MeV neutrons will reach the front face of the detectors in 156/5.1 = 30.6 ns. The detector crystal is 15.24 cm deep, which equates to approximately 3 ns of travel time for a 14.1 MeV neutron. In order to account for directly transmitted neutrons interacting anywhere in the detector crystal, the total number of neutrons from 30-34 ns (region 2) will be summed to determine the number of directly transmitted fast neutrons for each simulated source-detector correlation.

The modeled DT neutron fan contains approximately 3.47×10^{-3} of the total solid angle. The DT generator is assumed to produce 3×10^7 neutrons per second isotropically, and the alpha detector is assumed to have an efficiency of approximately 85%, which is the approximate efficiency of the alpha detector currently in use on the DT generator. [13] Multiplying these three values together, 8.85×10^4 source neutrons are produced in the neutron fan per second of measurement time. Thus, each MCNP-PoliMi input deck will have a source term of:

$$nps = \left(8.85 \times 10^4 \ {}^{n}\!\!\big/\!{}_{s}\right) \times t_{sample} \tag{7}$$

where nps is the MCNP-PoliMi input card which dictates the number of source particles produced, and t_{sample} is the measurement time per sample.

As discussed in Section 2.4, a typical NMIS sample time is a multiple of 5.12 seconds. In order to match the MCNP-PoliMi simulations with the physical NMIS configuration, each individual simulation was given a source term (nps card) that was an even multiple of $8.85 \times 10^4 \times 5.12$ s = 4.53×10^5 neutrons. Each simulated scan consists of 44 samples, which equates to 225 s (3.75 min) of total measurement time (excluding the time required to move the source and detectors between each sample). For all test cases, values of 1, 4, and 10 5.12 second loops will be used to compare the effects of different simulated measurement times on the accuracy of the simulated measurements.

4.3 Simulated Reference Scans

As in a physical NMIS scan, when the goal is to examine the contents of a container this is best accomplished by first scanning an empty container and subtracting it away to determine the net effect of the material inside. Thus, the first simulated scan was made of an empty container. In addition to the reference scan of the empty container, a second reference scan was simulated using a container with a known density profile. This second reference scan assumes that a UO_3 container could first be scanned full, then emptied and scanned again. After emptying the container, the material inside could be weighed and the approximate density profile could be determined based on the relative neutron transmissions through each pixel. However, for the purposes of this paper, the full reference scan will be assumed to be completely filled with UO_3 powder having a uniform density of 8.00 g/cm^3.

Because the results of the scans will be used with all future measurements, it is desirable that they be as accurate as possible to reduce any bias in the calculated values. Thus, both the empty container ('void') and full, uniform container ('rho=8') scans were designed to simulate very

long NMIS scans. These simulations correspond to NMIS measurements consisting of 10 loops, 10^8 blocks per loops, and a 512 ns block size. Using this data, equation 6 produces a sample time of 512 sec, or 8.53 min. Each scan consists of a total of 44 samples, so each simulation corresponds to a total of 375 min, or 6.26 hrs, which would represent correspond to an all day or over night measurement. From equation 7, the source (nps) card in MCNP-PoliMi for each sample is 4.53×10^7 neutrons.

In order to minimize the possibility that a particular random seed could unduly skew the simulations, each of the reference scans were broken into three input decks, each of which used a different random seed and stride. After the simulations were completed using all three random numbers, they were recombined into a single measurement, which was then postprocessed, as was described in Section 4.2.

Once the reference scans were post-processed, the resulting output is the number of correlations in the fast neutron peak, per source neutron, for each pixel. Table 1 below shows a small sample of these results for both the 'void' and 'rho=8' cases.

Table 1   **Sample results showing the normalized number of correlations in the fast neutron peak for several detector positions.**

Void Scan, $I_0^{i,j}$					
	Detector 21	Detector 22	Detector 23	Detector 24	Detector 25
Slice 10	5.17E-04	5.17E-04	5.18E-04	5.10E-04	5.21E-04
Slice 11	5.17E-04	5.16E-04	5.18E-04	5.09E-04	5.21E-04
Slice 12	5.17E-04	5.16E-04	5.18E-04	5.08E-04	5.20E-04
Slice 13	5.16E-04	5.16E-04	5.17E-04	5.08E-04	5.20E-04
Slice 14	5.18E-04	5.18E-04	5.18E-04	5.10E-04	5.22E-04

Rho=8 Scan, $I_8^{i,j}$					
	Detector 21	Detector 22	Detector 23	Detector 24	Detector 25
Slice 10	9.34E-05	9.43E-05	9.16E-05	9.36E-05	9.49E-05
Slice 11	9.29E-05	9.44E-05	9.10E-05	9.28E-05	9.38E-05
Slice 12	9.24E-05	9.37E-05	9.13E-05	9.27E-05	9.31E-05
Slice 13	9.22E-05	9.36E-05	9.03E-05	9.21E-05	9.31E-05
Slice 14	9.18E-05	9.33E-05	9.08E-05	9.26E-05	9.30E-05

Each of these normalized correlation values will be designated by the symbol '$I^{i,j}$', where the subscript **i** represents the vertical slice and the subscript **j** represents the detector position. So, for example, $I^{12,24}$ represents the correlation value in the pixel defined by the 12th vertical slice and the 24th detector position. The correlation values of the two reference measurements will be give subscripts of 0 and 8 for the 'void' and 'rho=8' cases, respectively. Using these two values, the transmittance of 14.1 MeV neutrons through the UO_3 powder in pixel i,j is:

$$\frac{I_8^{i,j}}{I_0^{i,j}} = e^{-\Sigma_t x_{i,j}} \tag{8}$$

where Σ_t is the macroscopic total cross-section for 14.1 MeV neutrons in the UO_3 powder, and $x_{i,j}$ is the average path length through the UO_3 powder for pixel i,j. For a given isotope, the macroscopic cross-section can be computed using the formula:

$$\Sigma_t = \frac{\rho \cdot N_A}{M} \sigma_t \tag{9}$$

where ρ is the density, N_A is Avogadro's Number, 6.022×10^{23} atoms/mol, M is the isotopic mass, in g/mol, and σ_t is the microscopic total cross-section, in barns, where 1 barn = 10^{-24} cm². Substituting equation 9 into equation 8 produces:

$$\frac{I_8^{i,j}}{I_0^{i,j}} = e^{-\frac{\rho_8 \cdot N_A}{M} \sigma_t \cdot x_{i,j}} \tag{10}$$

Where p_8 is the density of the UO_3 powder in the 'rho=8' scan, which is defined as 8.00 g/cm³. M and σ_t are determined by the physical properties of the UO_3 powder and will remain constant. Similarly, the $x_{i,j}$'s depend solely on the geometry of the pixel and will remain constant from one simulated scan to another. Thus, equation 10 can be rewritten as:

$$\frac{I_8^{i,j}}{I_0^{i,j}} = e^{-b_{i,j} \cdot \rho_8} \tag{11}$$

where

$$b_{i,j} = \frac{N_A \cdot \sigma_t \cdot x_{i,j}}{M} . \tag{12}$$

Solving equation 11 for the coefficient $b_{i,j}$ yields:

$$b_{i,j} = \frac{-\ln\left(\frac{I_8^{i,j}}{I_0^{i,j}}\right)}{\rho_8} \tag{13}$$

For example, for slice 12, detector position 24,

$$b_{12,24} = \frac{-\ln\left(\frac{9.27 \times 10^{-5}}{5.08 \times 10^{-4}}\right)}{8.00 \, g/cm^3} = 0.213 \, cm^3/g \tag{14}$$

If the attenuation of 14.1 MeV neutrons is governed by equation 8, and the fast neutron peaks consist exclusively of neutrons which have passed directly through the container without interaction, then there exists a linear relationship between the UO_3 density and the attenuation of

14.1 MeV neutrons in the powder. This attenuation, α, can be written in terms of mean free paths using the equation:

$$\alpha_{i,j} = -\ln\left(\frac{I^{i,j}}{I_0^{i,j}}\right) = \Sigma_t x = \frac{x}{\lambda}, \tag{15}$$

where λ is the mean free path of a 14.1 MeV neutron in the UO_3 powder. The mean free path, λ, represents the average distance a neutron is expected to travel before interacting. It also represents the distance in which an incident neutron field will be reduced to 1/e of its original strength. In this case, I represents a generic measurement of the correlations in the fast neutron peak. Substituting the values of I_0 and I_8 for I in equation 15 produces the two large data points shown in Figure 7, which represent the observed attenuation in UO_3 powder with densities of 0 g/cm^3 and 8.00 g/cm^3.
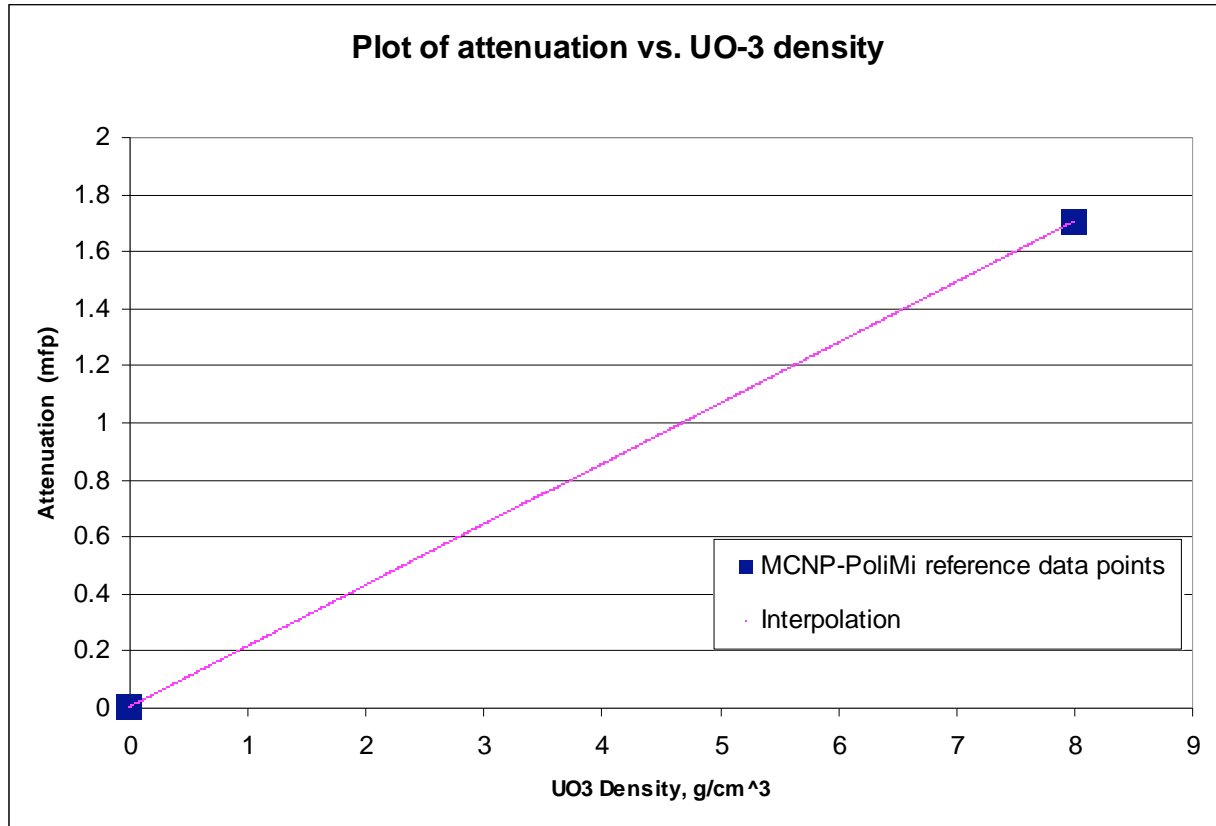
Figure 7　　　A plot of attenuation vs. UO_3 powder density consisting of two simulated points and an interpolation line between them

The values of I_0 and I_8 used to create Figure 7 above were those for pixel 12,24, which are listed in Table 1. The coefficient $b_{12,24}$, which was calculated to be 0.213 cm^3/g, is the slope of the interpolation line joining these two points. When a container that has an unknown configuration of UO_3 powder is scanned, the mean density in that pixel can be estimated by interpolating the attenuation value from the unknown measurement. For example, if the attenuation value is 1 mean free path, the estimated mean density is approximately 4.7 g/cm^3. Because the geometry of

the container is known, this mean density can then be multiplied by the volume of the interior of the container which the detector shadows to estimate the effective mass of that volume element.

Analytically, the average density of each pixel would be calculated using the equation:

$$\rho_{i,j} = \frac{\alpha_{i,j}}{b_{i,j}} \tag{16}$$

Substituting equations 13 and 15 into equation 16 yields:

$$\rho_{i,j} = \frac{-\ln\left(\dfrac{I_U^{i,j}}{I_0^{i,j}}\right)}{-\ln\left(\dfrac{I_8^{i,j}}{I_0^{i,j}}\right)}\rho_8 = \frac{\ln\left(I_U^{i,j}\right) - \ln\left(I_0^{i,j}\right)}{\ln\left(I_8^{i,j}\right) - \ln\left(I_0^{i,j}\right)}\rho_8 \tag{17}$$

Once the average density has been calculated for each pixel, the mass of the trough, M, can then be calculated using the equation:

$$M = V \sum_{i=1}^{22} \sum_{j=1}^{48} f_{i,j} \cdot \rho_{i,j} \tag{18}$$

Where $f_{i,j}$ is the fraction of the container volume that lies between the source and the detector face in the i,jth pixel. V is the volume of the container's interior. Substituting equation 17 into 18 yields:

$$M = \rho_8 \cdot V \sum_{i=1}^{22} \sum_{j=1}^{48} f_{i,j} \cdot \frac{\ln\left(I_U^{i,j}\right) - \ln\left(I_0^{i,j}\right)}{\ln\left(I_8^{i,j}\right) - \ln\left(I_0^{i,j}\right)} \tag{19}$$

4.4 Simulated Test Cases

In order to test the validity of equation 19 for determining the UO_3 powder mass inside of the container, three test cases were examined. In each case, it was assumed that the contents of the container being scanned were unknown. One of the underlying assumptions of equation 19 and the three that precede it is that so long as the average density within a pixel is the same, the attenuation will be the same, regardless of the actual configuration of the powder within the pixel. For example, a pixel that is half filled with a given density of UO_3 powder vertically will have the same average density as a pixel that is half filled horizontally. Figure 8 illustrates this graphically.
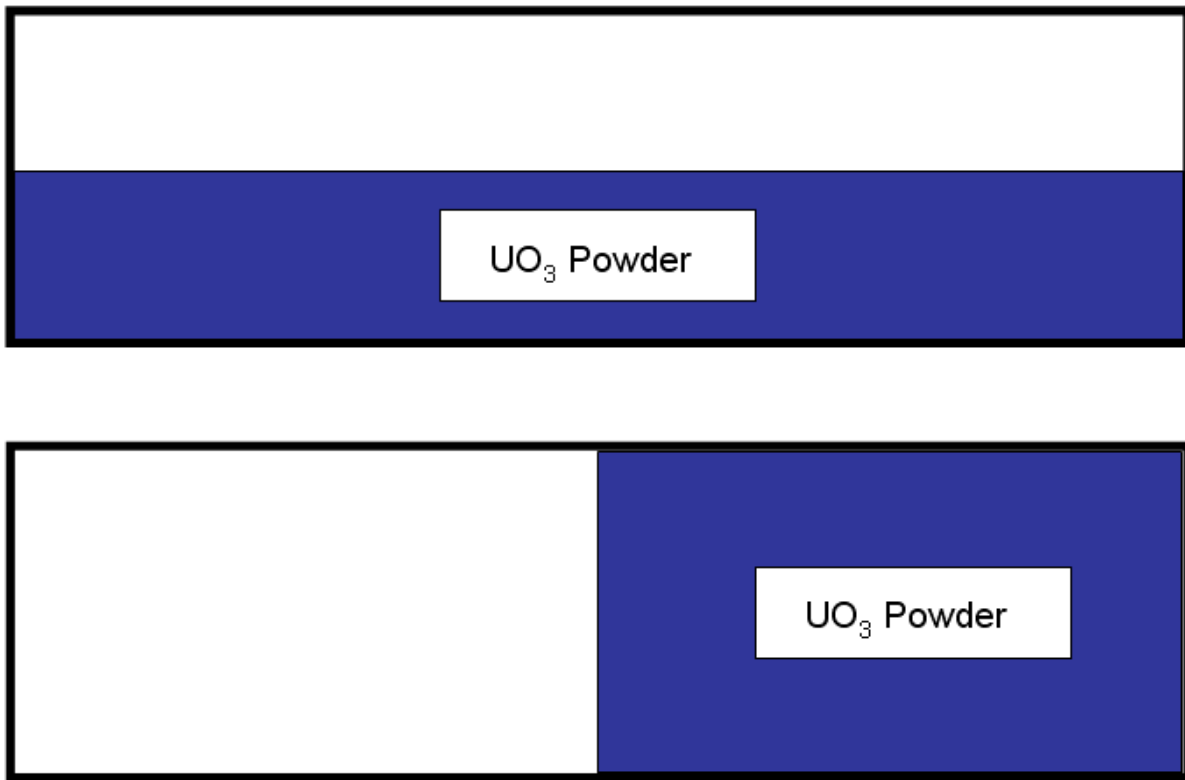
Figure 8   Two pixel configurations that have the same average density

In an attempt to test this assumption, the three test cases selected contained radically different UO_3 powder distributions. The first case contains 2 separate UO_3 powder densities layered one on top of the other. The lower layer has a density of 8.00 g/cm^3 and the upper a density of 7.00 g/cm^3. For the second case, the powder has a density of 8.00 g/cm^3 and its surface is sloped at and angle of approximately 30°. The upper portion of the container is empty in this case. The third and final case simulates a large air bubble within the powder. The bubble is modeled as a spherical void with a radius of 5 cm. The UO_3 powder in the rest of the container has a density of 8.00 g/cm^3. Figure 9 shows a cross-section of each of these three cases.
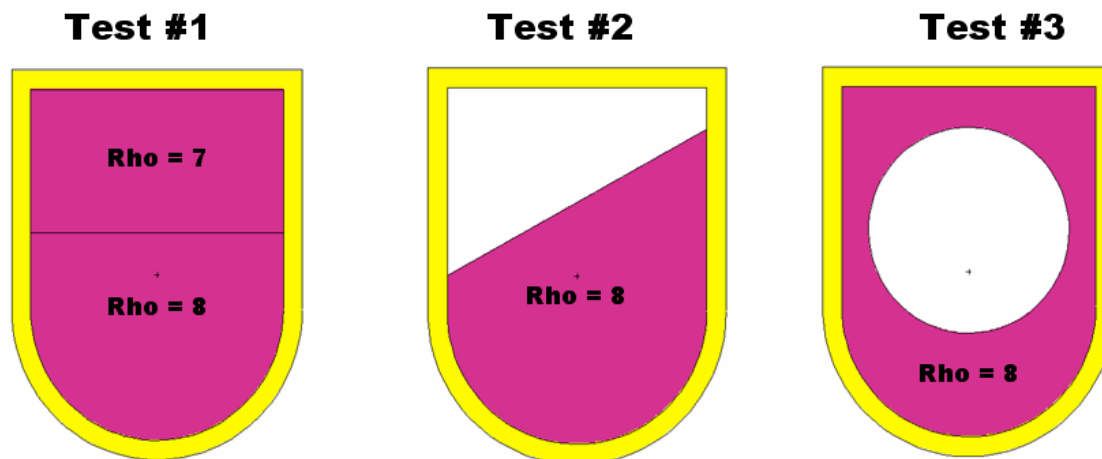
Figure 9   **The three test cases modeled in MCNP-PoliMi**

In order to test the effect of the simulated measurement time on the accuracy of the mass estimation, three different measurement times were simulated for each case. The three measurement times chosen were 5.12, 20.48, and 51.2 seconds per sample. These times correspond to $1x10^7$, $4x10^7$, and $1x10^8$ 512 ns blocks per sample, respectively. Multiplied by 44 samples per scan, the total scan would require 3.75, 15.0, and 37.5 minutes, neglecting the time required to reposition the scanning arm between samples. Using equation 7, the MCNP-PoliMi nps source card corresponding to each of these sample times is approximately $4.53x10^5$, $1.81x10^6$, and $4.53x10^6$ neutrons.

From shortest to longest, the measurement times will be designated by the letters a, b, and c attached to the case number. For example, Case 2a refers to a simulation using Case 2 as the container model with an nps card of $1.81x10^6$ neutrons.

5. Results

After each of the nine unknown simulations was run, the UO_3 mass was estimated using the equations from Sections 4.3 and 4.4. Sections 5.1 – 5.3 show the results of the longest simulation for each case (the 'c' cases) graphically. Section 5.4 then shows the results for all nine simulations and compares these results with known values to determine the accuracy of the method used to determine the UO_3 mass.

5.1 Case 1c

The geometry of case 1 consists of a layer of 7.00 g/cm^3 powder on top of a layer of 8.00 g/cm^3 powder. Figure 10 below shows the number of normalized correlations in each pixel, as measured by the simulation of case 1c. Note that while the four stainless steel walls are clearly visible, the powder inside of the container looks almost completely homogeneous. Similar figures for cases 1a and 1b would appear almost identical, save for the fact there would be a greater variation between similar pixels.
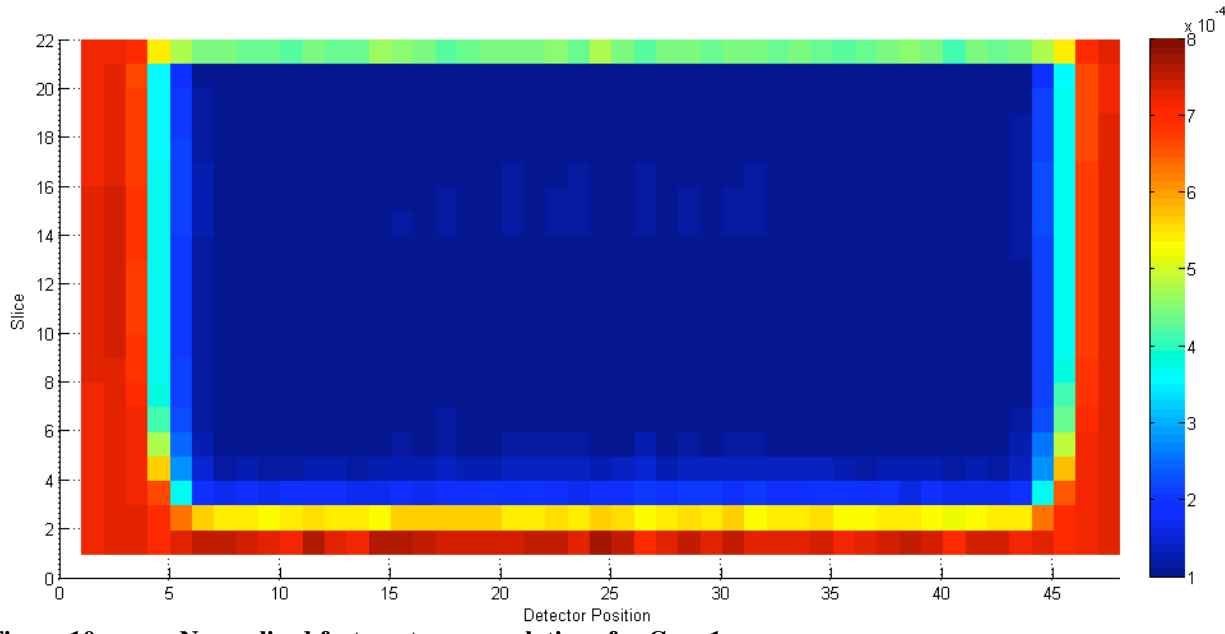
Figure 10   **Normalized fast neutron correlations for Case 1c**

In Figure 11 below, the correlations from Figure 10 have been converted to attenuation values using equation 15 with the $I_U^{i,j}$ values substituted in. Notice that the container walls have completely vanished in this picture, and only the calculated attenuation values of the UO$_3$ powder remain. The bottom half of the powder appears to be visibly darker than the top, and a darker horizontal band corresponding to slice 13 runs across the middle of the container. This band corresponds to the slice directly above the division between the two density layers.
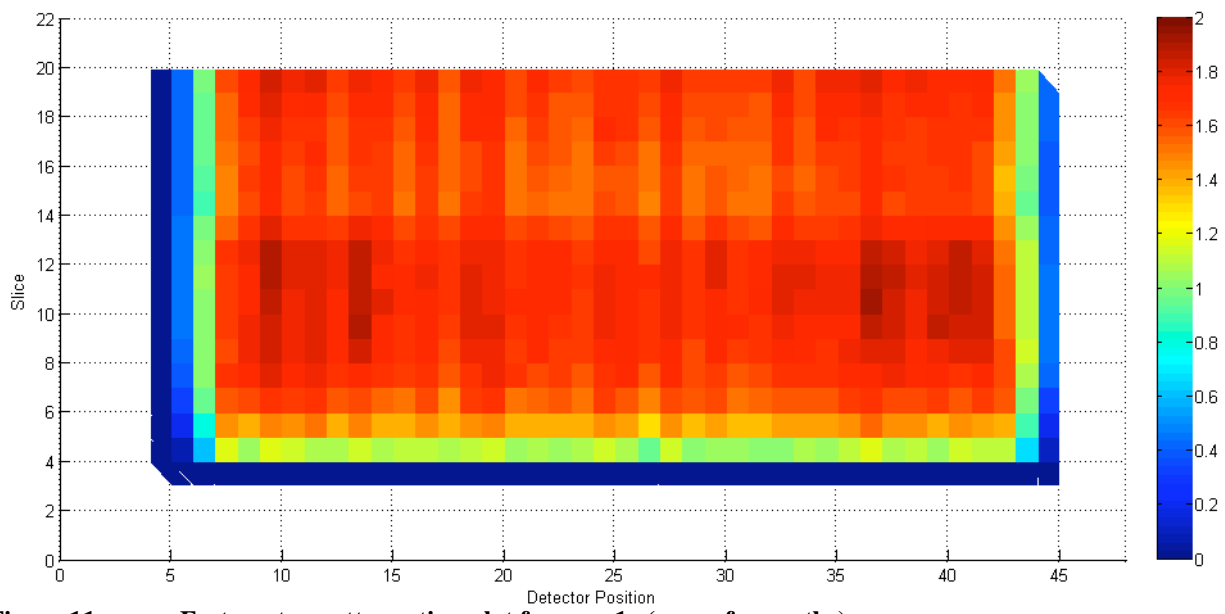
Figure 11   **Fast neutron attenuation plot for case 1c (mean free paths)**

In Figure 12 the attenuation values from Figure 11 have been converted to densities using equation 17. The disparity between the two layers is slightly more visible in the density plot than in the preceding figure.
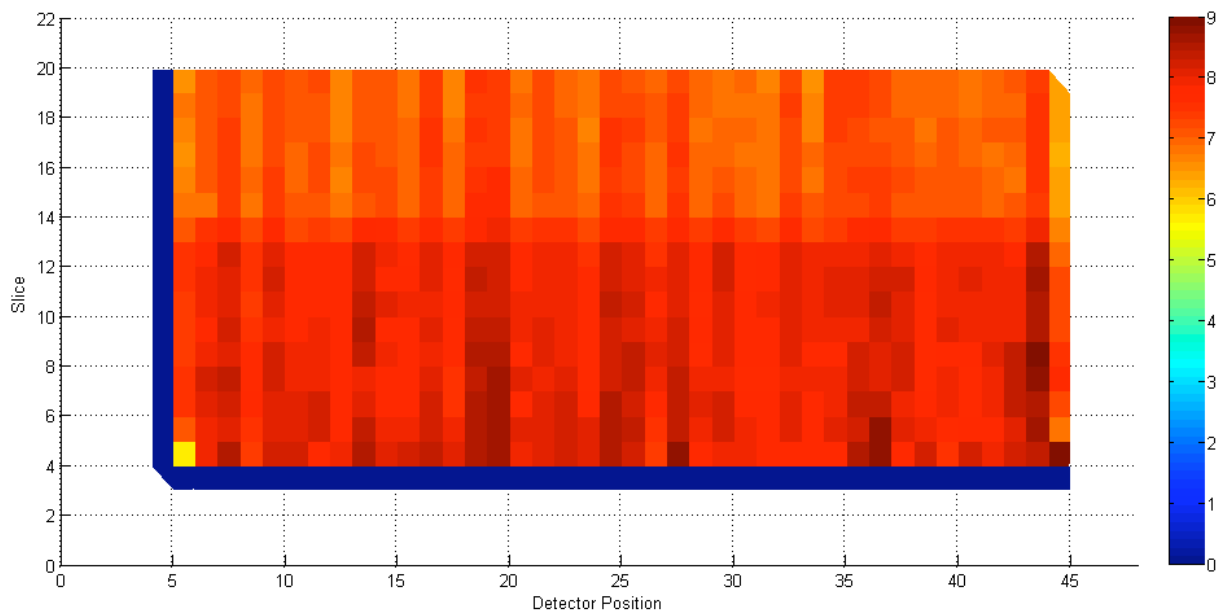
Figure 12   **Density plot for case 1c (g/cm^3)**

5.2 Case 2c

Figure 13 shows the correlation rates for case 2c. In this case, the UO$_3$ powder is sloped at an angle of ~30°, beginning just below slice 11 and ending above slice 17. Unlike case 1c, this geometry is clearly visible with just the unknown correlation data.
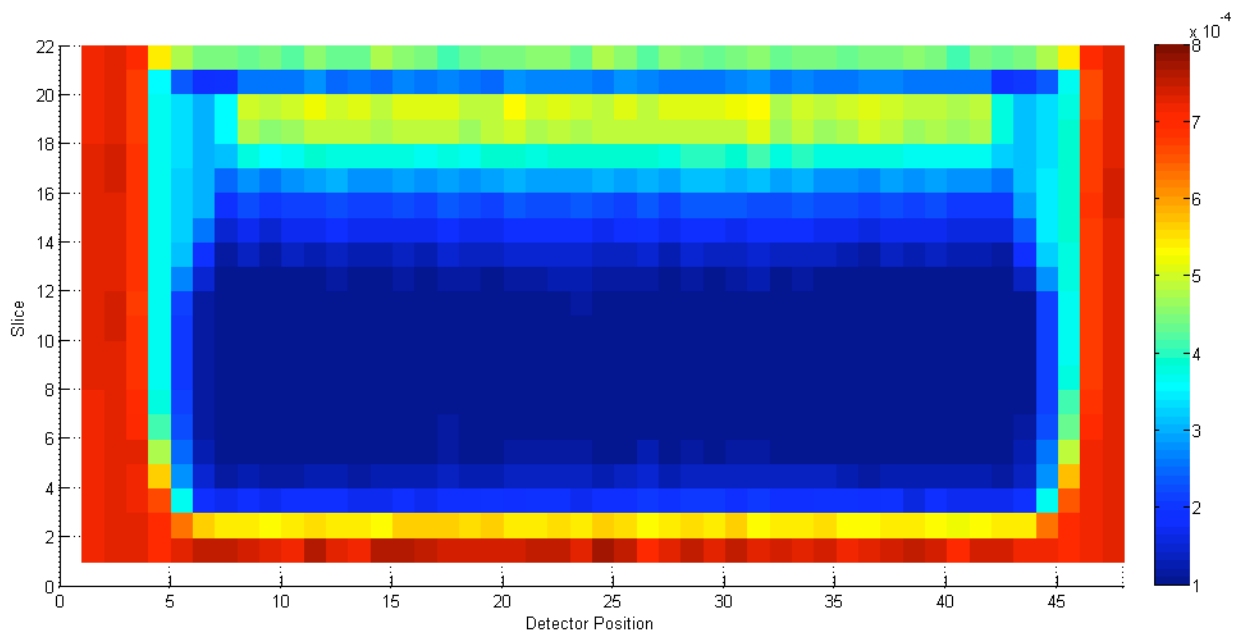
Figure 13   **Normalized fast neutron correlations for Case 2c**

Figure 14 shows the attenuation values of case 2c. The slope of the powder from slice 11 to 18 is clearly visible, and the completely full area at the bottom of the container stands out in sharp contrast to the sloping area.
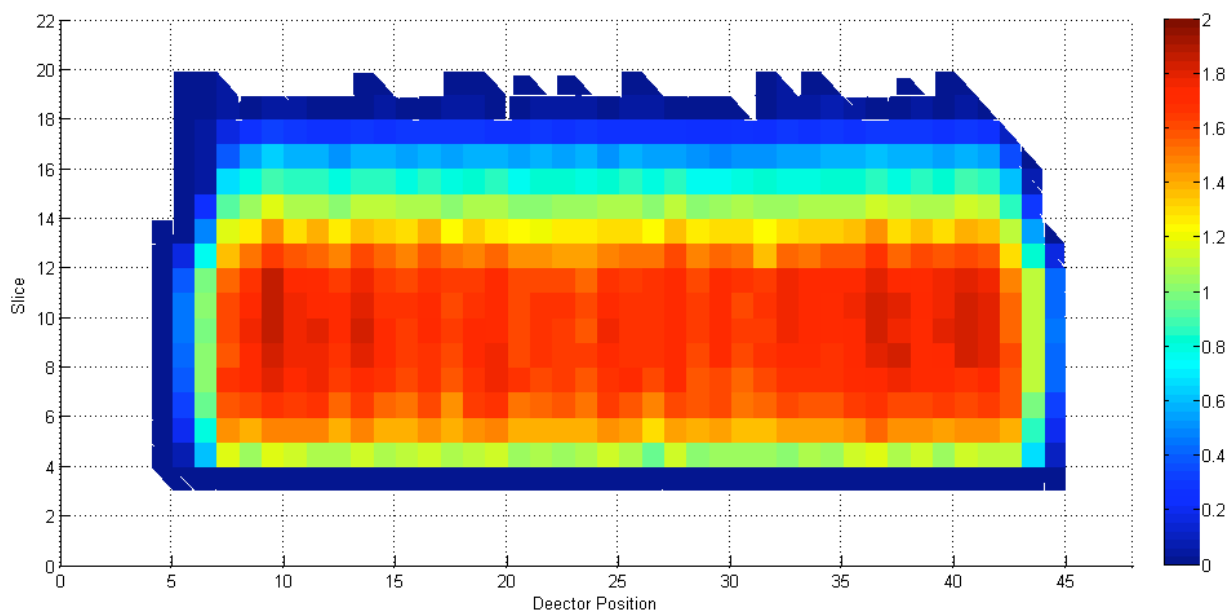
Figure 14   **Fast neutron attenuation plot for case 2c (mean free paths)**

Figure 15 shows the calculated densities for case 2c. Again, the slope of the powder inside of the container is clearly visible.
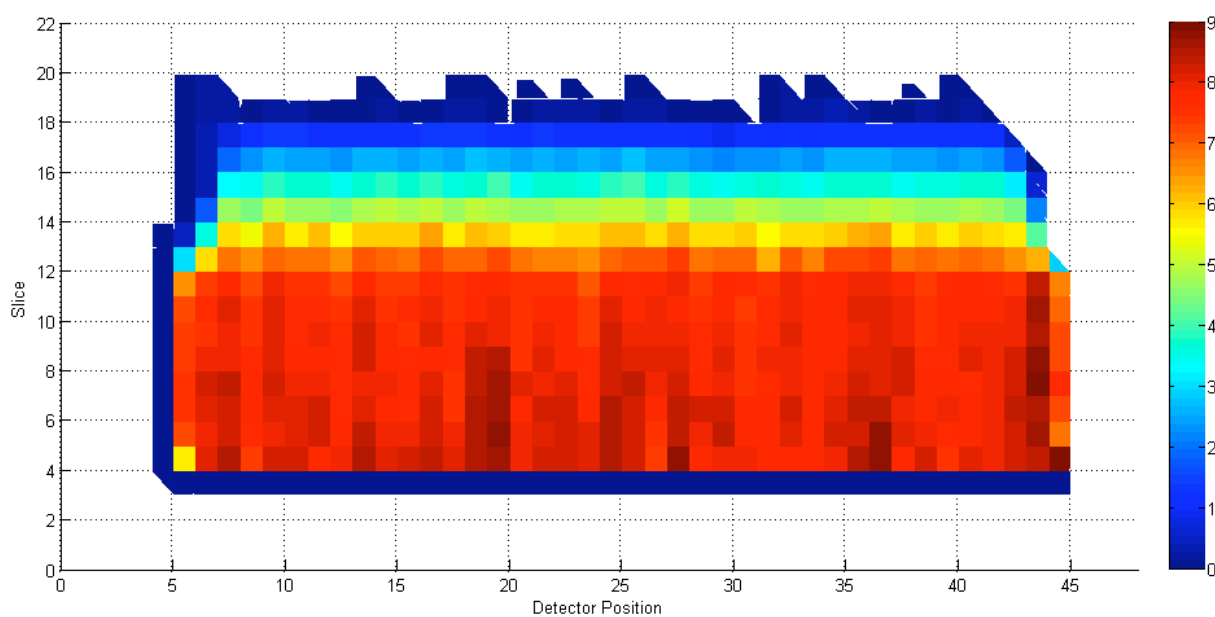
Figure 15   **Density plot for case 2c (g/cm³)**

5.3 Case 3 –

Case 3 simulates a large, 10 cm diameter, air bubble inside of the UO_3 powder. This air bubble is centered in the container horizontally and centered between pixels 13 and 14 vertically. In Figure 16, the air bubble is clearly visible in a plot of raw correlation rates.
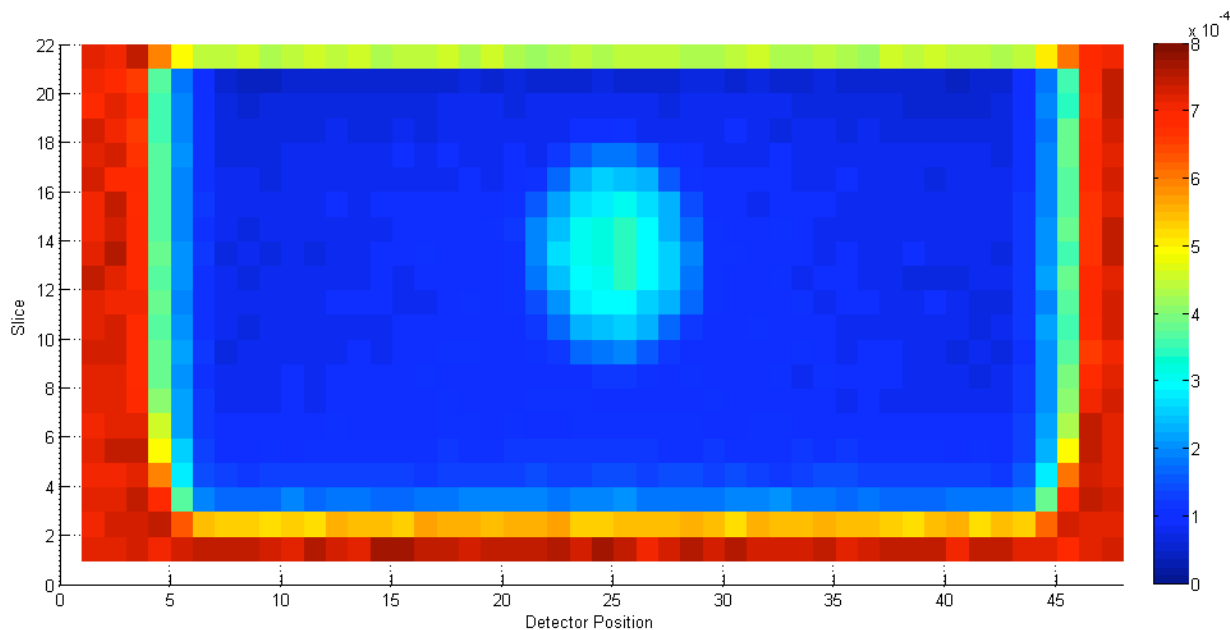
Figure 16   **Normalized fast neutron correlations for Case 3c**

Figure 17 shows the attenuation values calculated from the case 3c simulation. The bubble is clearly visible in this picture.
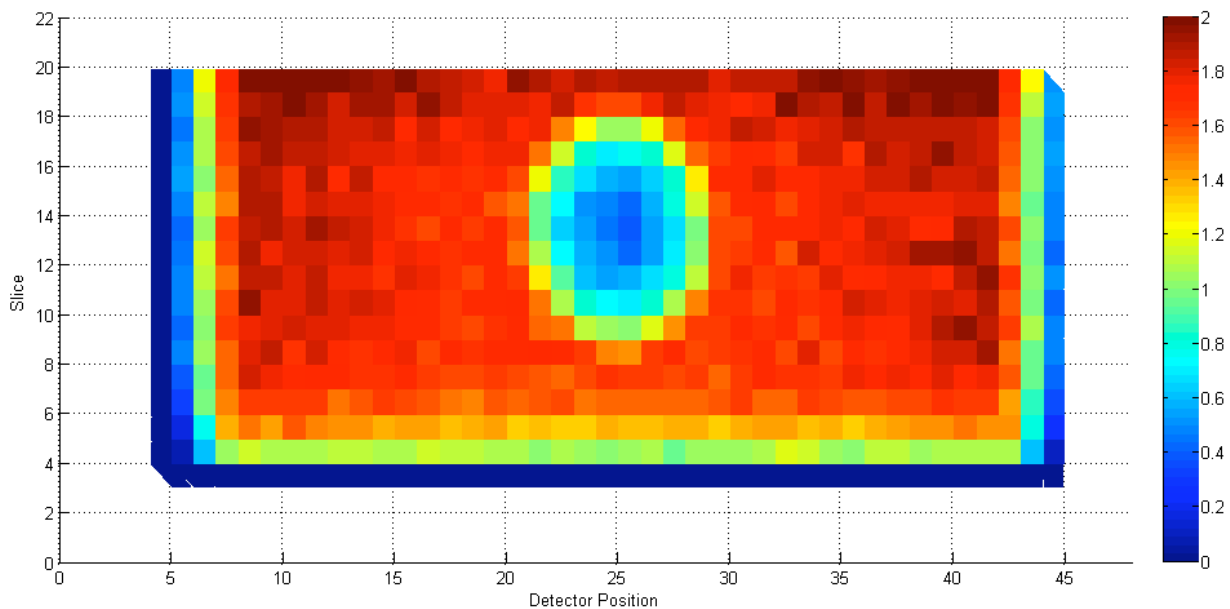
Figure 17   **Fast neutron attenuation plot for case 3c (mean free paths)**

In Figure 18 the air bubble is clearly visible in a plot of the calculated pixel densities.
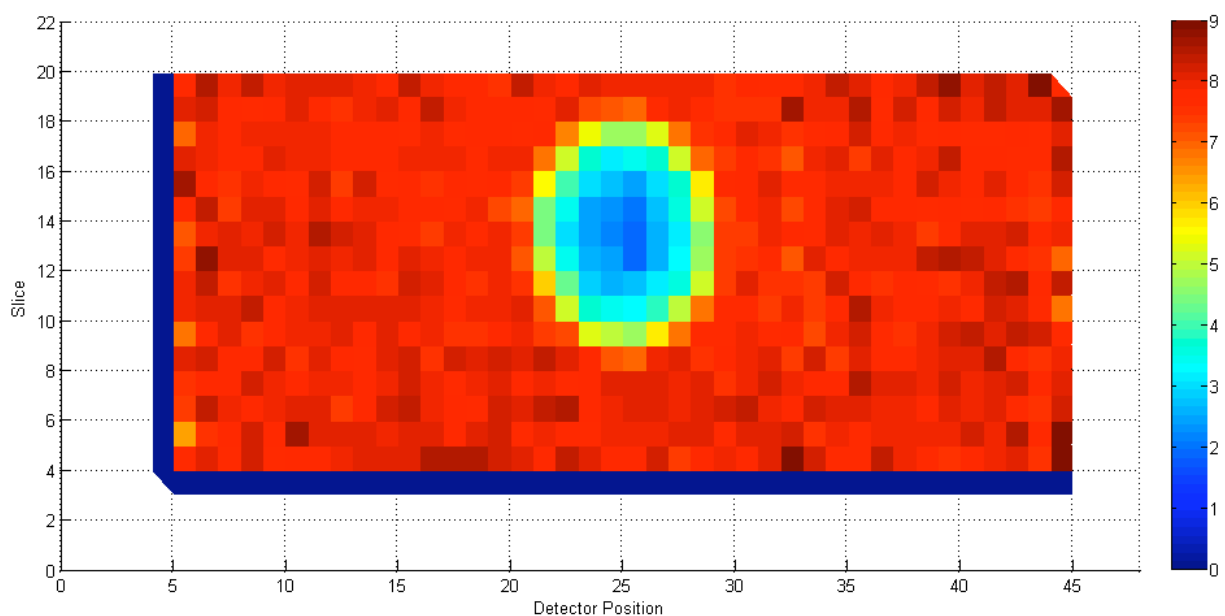
Figure 18   **Density plot for case 3c (g/cm^3)**

5.4 Summary

Table 2, below, shows the results of the 9 simulated measurements conducted on unknown containers. The measurement time column shows the time, in minutes, to conduct the corresponding scan on the actual NMIS system. The column labeled true mass shows the actual mass of UO$_3$ in a container matching the geometry defined for that case. The estimated mass is the result of each simulation, as calculated using equation 19. Finally, the fractional error column shows the deviation of the estimated mass from the true mass as a function of the percentage of true mass.

Table 2   **Summary of simulation results**

Case Number	Measurement Time (min)	True Mass (kg)	Estimated Mass (kg)	Fractional Error
1a	3.75	65.812	65.982	+0.0026
1b	15.02	65.812	66.772	+0.0146
1c	37.55	65.812	66.290	+0.0073
2a	3.75	45.339	46.329	+0.0218
2b	15.02	45.339	46.698	+0.0300
2c	37.55	45.339	46.302	+0.0213
3a	3.75	65.502	65.838	+0.0051
3b	15.02	65.502	65.298	-0.0031
3c	37.55	65.502	64.909	-0.0091

All of the estimated masses shown in Table 2 are within 3% of the true value. This suggests that the algorithm used to calculate the mass is relatively accurate, at least with respect to the three modeled geometries and geometries that are similar to those. Most of the 9 mass estimates are larger than the true masses, suggesting the possibility of a systematic error which is causing the algorithm to produce measurements which are higher than the true value. The three simulations of case 2, in particular, appear to be systematically high. However, in order to verify this observation, the uncertainty of the mass estimates needs to be calculated. Once the uncertainties are known, they can be compared to the fractional error in order to determine if the mass estimates are abnormally high, or if they can be attributed to random fluctuations about the mean. The hypothesis that there is no systematic error can be rejected only if the absolute value of the fractional error is several times larger than the fractional uncertainty. This uncertainty will be quantified in Section 6.

6. Uncertainty Analysis

The results listed in chapter 5 represent only one possible mass estimate from an unknown population. The mass measurement resulting from any given simulation could deviate from the one listed above in accordance with the underlying variance of the population. The next goal, then, is to attempt to characterize the uncertainty in the results of the 9 simulations. The most straightforward method would be to repeat each simulation several times. If the simulation were repeated N times, the population mean and variance could then be estimated using the equations:

$$\overline{M} = \frac{\sum_{k=1}^{N} M_k}{N} \tag{20}$$

and

$$s^2 = \frac{\sum_{k=1}^{N} \left(M_k - \overline{M} \right)^2}{N-1} \tag{21}$$

where M_k is the mass estimate produced by the kth simulation, $\overline{M}$ is the observed mean mass of the sample, and s^2 is the observed variance of the sample.

Unfortunately, because each simulation requires several hours to several days of computing time, repeating every simulation several times is impractical. Rather than repeating the simulation several times, two point estimation methods will be employed in order to estimate the variance in the results from single simulations listed in chapter 4. These two methods are an analytical propagation of variance using Gauss's Error law, and a Monte Carlo error propagation technique. In addition to estimating the uncertainty, a third section will quantify how the presence of a high background count rate would affect the results.

6.1 Propagation of Variance Method

The goal of the Propagation of Variance method is to estimate the uncertainty of the output variable, UO_3 powder weight in this case, given a known variation in the input variables. The input variables are the individual source-detector correlations from each individual scan. Thus, there are 3 input variables per pixel, multiplied by 1056 pixels, for a total of 3168 input variables. Each correlation was calculated by dividing the number of counts within the fast neutron peak by the number of source particles. By multiplying these values by the number of source particles (in effect undoing the normalization), the correlations are converted to a number of counts. These values can then be treated using standard counting statistics, in which the detected counts are assumed to follow a Gaussian distribution, which has a variance equal to its mean.

If the standard deviation of each input variable is relatively small compared to its mean, and if no correlation exists between the input variables, the variance of the output variable can be calculated using the Gaussian Error Approximation: [8]

$$\sigma_u^2 = \left(\frac{\partial u}{\partial x}\right)^2 \sigma_x^2 + \left(\frac{\partial u}{\partial y}\right)^2 \sigma_y^2 + \left(\frac{\partial u}{\partial z}\right)^2 \sigma_z^2 + ... \tag{22}$$

Here, the variance will be propagated in a two step phase. In the first, the variance of the UO_3 powder density in each pixel will be calculated. Then, these individual density variances will be propagated to calculate the variance in the mass of the powder. In order to apply the counting statistics to the density formula (Equation 17), it needs to be rewritten in the form:

$$\rho_{i,j} = \frac{\ln\left(\frac{C_U^{i,j}}{N_U^{i,j}}\right) - \ln\left(\frac{C_0^{i,j}}{N_0^{i,j}}\right)}{\ln\left(\frac{C_8^{i,j}}{N_8^{i,j}}\right) - \ln\left(\frac{C_0^{i,j}}{N_0^{i,j}}\right)} \rho_8 = \frac{\ln\left(C_U^{i,j}\right) - \ln\left(C_0^{i,j}\right) - \ln\left(N_U^{i,j}\right) + \ln\left(N_0^{i,j}\right)}{\ln\left(C_8^{i,j}\right) - \ln\left(C_0^{i,j}\right) - \ln\left(N_8^{i,j}\right) + \ln\left(N_0^{i,j}\right)} \rho_8 \tag{23}$$

where $C^{i,j}$ represents the total counts under the fast neutron peak for the i,jth pixel and N represents the source term for each of the simulations, as denoted by the subscripts. Since the N terms are constants, the uncertainty in the density of a given pixel can be expressed as:

$$\sigma_\rho^2 = \left(\frac{\partial \rho}{\partial C_U}\right)^2 \sigma_{C_U}^2 + \left(\frac{\partial \rho}{\partial C_0}\right)^2 \sigma_{C_0}^2 + \left(\frac{\partial \rho}{\partial C_8}\right)^2 \sigma_{C_8}^2 \tag{24}$$

Note that although the i,j superscripts have been omitted for clarity, this value must be computed separately for each pixel. This superscript will also be omitted from further propagation of variance calculations for the density. The three partial derivatives in equation 24 are:

$$\frac{\partial \rho}{\partial C_U} = \frac{1}{C_U \cdot \ln\left(\frac{C_8 \cdot N_0}{C_0 \cdot N_8}\right)} \rho_8 , \tag{25}$$

$$\frac{\partial \rho}{\partial C_0} = \frac{\ln\left(\frac{C_U \cdot N_8}{C_8 \cdot N_U}\right)}{C_0 \cdot \ln^2\left(\frac{C_8 \cdot N_0}{C_0 \cdot N_8}\right)} \rho_8 , \text{ and} \tag{26}$$

$$\frac{\partial \rho}{\partial C_8} = \frac{-\ln\left(\frac{C_U \cdot N_0}{C_0 \cdot N_U}\right)}{C_8 \cdot \ln^2\left(\frac{C_8 \cdot N_0}{C_0 \cdot N_8}\right)} \rho_8 \tag{27}$$

Substituting equations 25-27 into equation 24 yields:

$$\therefore \sigma_\rho^2 = \left(\frac{1}{C_U \cdot \ln\left(\frac{C_8 \cdot N_0}{C_0 \cdot N_8}\right)} \rho_8\right)^2 \cdot \sigma_{C_U}^2 + \left(\frac{\ln\left(\frac{C_U \cdot N_8}{C_8 \cdot N_U}\right)}{C_0 \cdot \ln^2\left(\frac{C_8 \cdot N_0}{C_0 \cdot N_8}\right)} \rho_8\right)^2 \cdot \sigma_{C_0}^2 + \left(\frac{-\ln\left(\frac{C_U \cdot N_0}{C_0 \cdot N_U}\right)}{C_8 \cdot \ln^2\left(\frac{C_8 \cdot N_0}{C_0 \cdot N_8}\right)} \rho_8\right)^2 \cdot \sigma_{C_8}^2 \tag{28}$$

Because the assumed distribution has a variance equal to its mean, we can substitute the count rates for the variance. Performing this substitution and squaring the terms in the brackets of equation 28 produces:

$$\sigma_\rho^2 = \frac{C_U}{C_U^2 \cdot \ln^2\left(\frac{C_8 \cdot N_0}{C_0 \cdot N_8}\right)} \rho_8^2 + \frac{C_0 \cdot \ln^2\left(\frac{C_U \cdot N_8}{C_8 \cdot N_U}\right)}{C_0^2 \cdot \ln^4\left(\frac{C_8 \cdot N_0}{C_0 \cdot N_8}\right)} \rho_8^2 + \frac{C_8 \cdot \ln^2\left(\frac{C_U \cdot N_0}{C_0 \cdot N_U}\right)}{C_8^2 \cdot \ln^4\left(\frac{C_8 \cdot N_0}{C_0 \cdot N_8}\right)} \rho_8^2 \tag{29}$$

$$\sigma_\rho^2 = \frac{C_0 \cdot C_8 \cdot \ln^2\left(\frac{C_8 \cdot N_0}{C_0 \cdot N_8}\right) + C_U \cdot C_8 \cdot \ln^2\left(\frac{C_U \cdot N_8}{C_8 \cdot N_U}\right) + C_U \cdot C_8 \cdot \ln^2\left(\frac{C_U \cdot N_0}{C_0 \cdot N_U}\right)}{C_U \cdot C_0 \cdot C_8 \cdot \ln^4\left(\frac{C_8 \cdot N_0}{C_0 \cdot N_8}\right)} \rho_8^2 \tag{30}$$

Applying equation 22 to equation 18, the variance in the UO$_3$ mass would be:

$$\sigma_M^2 = V^2 \sum_{i=1}^{22} \sum_{j=1}^{48} f_{i,j}^2 \cdot \sigma_{\rho_{i,j}}^2 \tag{31}$$

The uncertainty of the mass is most conveniently expressed in terms of its standard deviation, which is computed by taking the square root of the right hand side of equation 31:

$$\sigma_M = V \sqrt{\sum_{i=1}^{22} \sum_{j=1}^{48} f_{i,j}^2 \cdot \sigma_{\rho_{i,j}}^2} \tag{32}$$

The fractional standard deviation represents the size of the uncertainty normalized to the mean value. The fractional uncertainty can be calculated using the formula:

$$\tilde{\sigma}_M = \frac{\sigma_M}{M} \tag{33}$$

Table 3, below, shows the true mass, measured mass, propagation of variance uncertainty, fractional uncertainty, and fractional error for each of the 9 scans.

Table 3   Summary of Propagation of Variance uncertainties

Case Number	True Mass (kg)	Estimated Mass (kg)	Uncertainty (kg)	Fractional Uncertainty	Fractional Error
1a	65.812	65.982	0.341	0.0052	+0.0026
1b	65.812	66.772	0.146	0.0022	+0.0146
1c	65.812	66.290	0.074	0.0011	+0.0073
2a	45.339	46.329	0.318	0.0069	+0.0218
2b	45.339	46.698	0.139	0.0030	+0.0300
2c	45.339	46.302	0.070	0.0015	+0.0213
3a	65.502	65.838	0.333	0.0051	+0.0051
3b	65.502	65.298	0.145	0.0022	-0.0031
3c	65.502	64.909	0.074	0.0011	-0.0091

Because the uncertainty is assumed to have a Gaussian distribution, it is possible to estimate the probability of randomly selecting the measured mass that listed in the third column of Table 3, assuming that the population mean is the same as the true mass of UO_3 powder in the container. The z-score would be:

$$z = \frac{\varepsilon_M}{\tilde{\sigma}_M} \tag{34}$$

where ε_M is the fractional error of the measurement, which was calculated using the formula:

$$\varepsilon_M = \frac{M_{measured} - M_{true}}{M_{true}} \tag{35}$$

For example, for Case 2c, $\tilde{\sigma}_M = 0.0015$ and $\varepsilon_M = +0.0213$. The z-score for this measurement is 14.2, which means that the fractional error is 14.2 times larger than the estimated uncertainty. The odds of selecting a measurement with such an extreme divergence from the mean given a normal distribution are approximately 1 in 10^{45}. Thus, a good deal of the error between the true mass and the measured mass in that particular simulation must be the result of systematic error rather than random error.

6.2 Monte-Carlo Method

The second method of uncertainty analysis is more straightforward than the Propagation of Variance method. The Monte Carlo method simulates multiple scans of the unknown container by randomly varying the input variables and calculating the resulting UO_3 mass. As in the previous section, the input variables will be the total number of correlations in the fast neutron peak for each pixel. Each number of correlations will be assumed to be sampled from a Gaussian distribution with a mean and variance equal to the number of correlations detected in the simulation. For each iteration, all of the input variables are randomly selected from their distributions and the mass is calculated. This process is repeated many times, generating a series of masses. This series of mass estimates can then be used to directly calculate the uncertainty in the mass.

The procedure described above was implemented using a custom Fortran-90 code. The Fortran-90 compiler generates random numbers from a Uniform(0,1] distribution. Because the input variables are assumed to be normally distributed, the following algorithm was used to generate a random normal:

$$\left[\sum_{k=1}^{12} j_k - 6 \right] \sim Norm(0,1) \tag{36}$$

where j_k is a random number drawn from a Uniform(0,1] distribution. The random value for each of the input correlations is then:

$$\hat{C}_m = C + \sqrt{C} \left[\sum_{k=1}^{12} j_k - 6 \right] \tag{37}$$

where the index m represents the mth Monte Carlo iteration. The mth sample mass, $\hat{M}_m$, would then be calculated using equations 23 and 18. If the process is iterated q times, the sample standard deviation of the mass is:

$$s_M = \sqrt{\frac{q}{q-1} \left[\sum_{m=1}^{q} \hat{M}_m^2 - \left(\sum_{m=1}^{n} \hat{M}_m \right)^2 \right]} \tag{38}$$

This process is similar to the one described at the beginning of Section 6. However, rather than repeating the original MCNP-PoliMi simulation many times to generate a sample of masses, this distribution was generated by randomly sampling input variables distributed around the nominal value from the simulation. Computationally, this method required significantly less input time. For example, a complete measurement consisting of the two long reference scans with $n=4.53\times10^7$ and an unknown scan with $n=4.53\times10^6$ required over a week to complete on a Pentium-4 2.27 GHz machine with 768 Mbytes of RAM. On the same machine, 10^6 iterations of the Monte Carlo uncertainty analysis program took slightly more than 1 hour.

Table 4 shows the results of the Monte Carlo uncertainty analysis for each of the simulated unknowns. These values were generated using a q of 10^6 iterations. The column entitled 'Mean Mass' is the sample mean of the distribution produced by the Monte Carlo code. The table also contains the fractional standard deviation derived from the Propagation of Variance method in Section 6.1 for comparison.

Table 4 **Summary of Monte Carlo uncertainties**

Case Number	True Mass (kg)	Estimated Mass (kg)	Mean Mass (kg)	MC Uncertainty (kg)	MC Fractional Uncertainty	PoV Fractional Uncertainty	Fractional Error
1a	65.812	65.982	66.493	0.268	0.0040	0.0052	+0.0026
1b	65.812	66.772	66.898	0.133	0.0020	0.0022	+0.0146
1c	65.812	66.290	66.340	0.086	0.0013	0.0011	+0.0073
2a	45.339	46.329	46.922	0.224	0.0048	0.0069	+0.0218
2b	45.339	46.698	46.907	0.112	0.0024	0.0030	+0.0300
2c	45.339	46.302	46.418	0.072	0.0015	0.0015	+0.0213
3a	65.502	65.838	66.369	0.272	0.0041	0.0051	+0.0051
3b	65.502	65.298	65.425	0.133	0.0020	0.0022	-0.0031
3c	65.502	64.909	64.960	0.086	0.0013	0.0011	-0.0091

The fractional uncertainties generated by both methods are within 50% of one another for all cases, indicating an approximate agreement between the two methods. For a Monte Carlo simulation, the mean of the sampled distribution should be approximately the same as the measured mass which was computed using the original (mean) input variables. That the mean masses generated with the Monte Carlo method are consistently higher than the measured mass indicates that the Monte Carlo method is biased to produce higher masses in this case. This size of this bias decreases for simulations with a larger source term. The most likely source of this bias is the underlying distribution of correlations that were input into the model. In some of the scans, the number of correlations in a particular pixel was as low as 17. Such a low number of counts is lower than should ideally be modeled with a normal distribution (values of 20-30 are typically recommended as the minimum). However, because this bias is less than ~2% in the worst of cases, the uncertainties calculated with this method should still be quite accurate.

6.3 Effects of Background Radiation

The MCNP-PoliMi simulations of NMIS measurements represent nearly ideal conditions. In physical measurements, there will likely be several possible sources of error. Most of these are

difficult to characterize, but one effect that can be modeled easily is the effect of background radiation on NMIS measurements. By the very nature of its primary target, namely fissile material, an NMIS scan is likely to be conducted in an area with a high background radiation count. Setting the detector thresholds fairly high (as described in Section 2.2) reduces the observed background count rate, but it could still be significant. This section will model the effects of these background counts on the simulated NMIS scans.

A rather robust background count rate of 5000 counts per second (cps) will be simulated in each the 24 plastic scintillators in the detector array. This is slightly higher than the count rate produced with a depleted uranium casting touching the detector face, which should approximately correspond to one of the highest background rates under which NMIS would be operated. No counts will be simulated in the alpha detector because it is very unlikely to detect background gamma rays because of its thin profile. In order to simplify calculations, it will be assumed that each source neutron is a completely independent event and that there is no overlap between one time correlation window and the next. If the correlation window of interest is about 200 ns after each alpha particle is detected, then the total time of interest for neutron-detector correlations in a 1 second period is:

$$t_{corr} = S \cdot t_{cw} = \left(8.85 \times 10^4 \, n\!/\!s\right)\left(200 \times 10^{-9} \, s\right) = 0.0177 \text{ seconds}, \tag{39}$$

where t_{corr} is the total time in which correlations are being examined, S is the count rate in the alpha detector, which corresponds to the neutron production rate in the neutron fan, and t_{cw} is the size of the correlation window for each source neutron. Since the total correlation time is less that 2% of the measurement time, the assumption of independence is quite reasonable.

In order to cause a possible error with an NMIS measurement, a background gamma ray must arrive during a time which would normally correspond to a directly transmitted fast neutron. For the purposes of this simulation, the fast neutron peak was 30 to 34 ns after the source neutron, a width of 5 ns. Only background radiation arriving during the time corresponding to these peaks will be significant. During a sample taken for time t_{sample}, and a fast neutron peak width of t_{peak}, the number of background counts meeting this criterion is:

$$C_{BG} = B \cdot t_{peak} \cdot S \cdot t_{sample} \tag{40}$$

where B is the background count rate, S is the alpha rate and C_{BG} is the number of measured coincidences due to the background. The IDAS software used with the NMIS system has the capability of subtracting out these accidental coincidences. However, because the number of counts observed in any given period will vary about the true mean, the deviation of the observed number of counts from the true mean will remain. The variation of observed number of counts is assumed to follow a Normal(C_{BG}, C_{BG}) distribution. In order to simulate the effect of these accidental coincidences, the number of correlations for each pixel in each scan will be sampled randomly using the following formula, which is a modified version of equation 37:

$$\hat{C}_m = C + \sqrt{C_{BG}}\left[\sum_{k=1}^{12} j_k - 6\right]$$ (41)

Equation 41 samples counts by varying the nominal number of counts from the PoliMi simulation normally with a variance equal to C_{BG}. For the three measurement times simulated in this report, C_{BG} equals 11.33, 45.31, and 113.3 accidental correlations per sample. By iterating this process q times, the uncertainty due to accidental coincidences caused by background radiation can be calculated. Table 5 shows the results of these calculations using $q=10^6$.

Table 5   Summary of uncertainty due to 5000 cps background radiation

Case Number	True Mass (kg)	Estimated Mass (kg)	Mean Mass (kg)	Background Uncertainty (kg)	Background Fractional Uncertainty	MC Fractional Uncertainty
1a	65.812	65.982	66.117	0.136	0.0021	0.0040
1b	65.812	66.772	66.805	0.068	0.0010	0.0020
1c	65.812	66.290	66.303	0.044	0.0007	0.0013
2a	45.339	46.329	46.585	0.107	0.0022	0.0048
2b	45.339	46.698	46.813	0.053	0.0011	0.0024
2c	45.339	46.302	46.377	0.034	0.0007	0.0015
3a	65.502	65.838	65.989	0.145	0.0022	0.0041
3b	65.502	65.298	65.333	0.070	0.0011	0.0020
3c	65.502	64.909	64.923	0.045	0.0007	0.0013

Note that the mean masses computed by the Monte Carlo background radiation simulations are higher than the nominal mass computed using the values directly from the simulations for all cases. This bias is similar, but smaller in magnitude, than the identical one observed in Section 6.2. Again, since the bias is quite small compared to the mean value, it should have a negligible effect on the uncertainty. Also, notice that the fractional uncertainty due to background radiation is consistently at approximately one-half of the corresponding fractional uncertainty due to uncertainty in the measured number of correlations. This is not surprising as both the number of accidental background correlations and true correlations both vary linearly with time for a given container geometry. The smaller magnitude of the background fractional uncertainty compared to the correlational uncertainty indicate that the accuracy of NMIS measurements should not be significantly affected by background counts, even in regions with high background radiation levels.

7. Conclusions

Table 6 summarizes the results of the nine simulated scans as well as the uncertainty of the estimate. Although two different methods were used to compute the uncertainty, only the results of the Monte Carlo analysis are presented here.

Table 6   Summary of simulation results and uncertainty analysis

Case Number	True Mass (kg)	Estimated Mass (kg)	Fractional Uncertainty	Fractional Error	z-score	Probability of Random

1a	65.812	65.982 ± 0.268	0.0040	+0.0026	+0.60	0.5485
1b	65.812	66.772 ± 0.133	0.0020	+0.0146	+7.30	< 0.0001
1c	65.812	66.290 ± 0.086	0.0013	+0.0073	+5.62	< 0.0001
2a	45.339	46.329 ± 0.224	0.0048	+0.0218	+4.54	< 0.0001
2b	45.339	46.698 ± 0.112	0.0024	+0.0300	+12.50	< 0.0001
2c	45.339	46.302 ± 0.072	0.0015	+0.0213	+14.2	< 0.0001
3a	65.502	65.838 ± 0.272	0.0041	+0.0051	+1.24	0.2150
3b	65.502	65.298 ± 0.133	0.0020	-0.0031	-1.55	0.1211
3c	65.502	64.909 ± 0.086	0.0013	-0.0091	-7.00	< 0.0001

The next to last column, the z-score, shows the number of standard deviations of the uncertainty that the error constitutes. The z-score is calculated using equation 34. The last column shows the probability that a randomly sampled mass estimate would produce the estimated mass, assuming that the mean of the distribution was the true mass.

With the exception of some of the shorter measurement times, all of the results indicate that there is virtually no probability that the errors in the estimates were due to random errors. Thus, the method used to produce the mass estimates generates mass estimates with a mean that differs from the actual mass in a statistically significant manner. The most likely source of this bias is the methodology used for determining the density of the UO_3 powder in a given pixel. This method assumes that, for a given pixel, the attenuation of 14.1 MeV neutrons is a linear function of the average density in that pixel. In an ideal case, where the neutrons are in a highly collimated narrow beam, and the detector occupies only a small portion of the total solid angle, this assumption is true. The upper line on Figure 19 shows such a relationship, which was computed using the cross-section values for 14.1 MeV neutrons in UO_3.
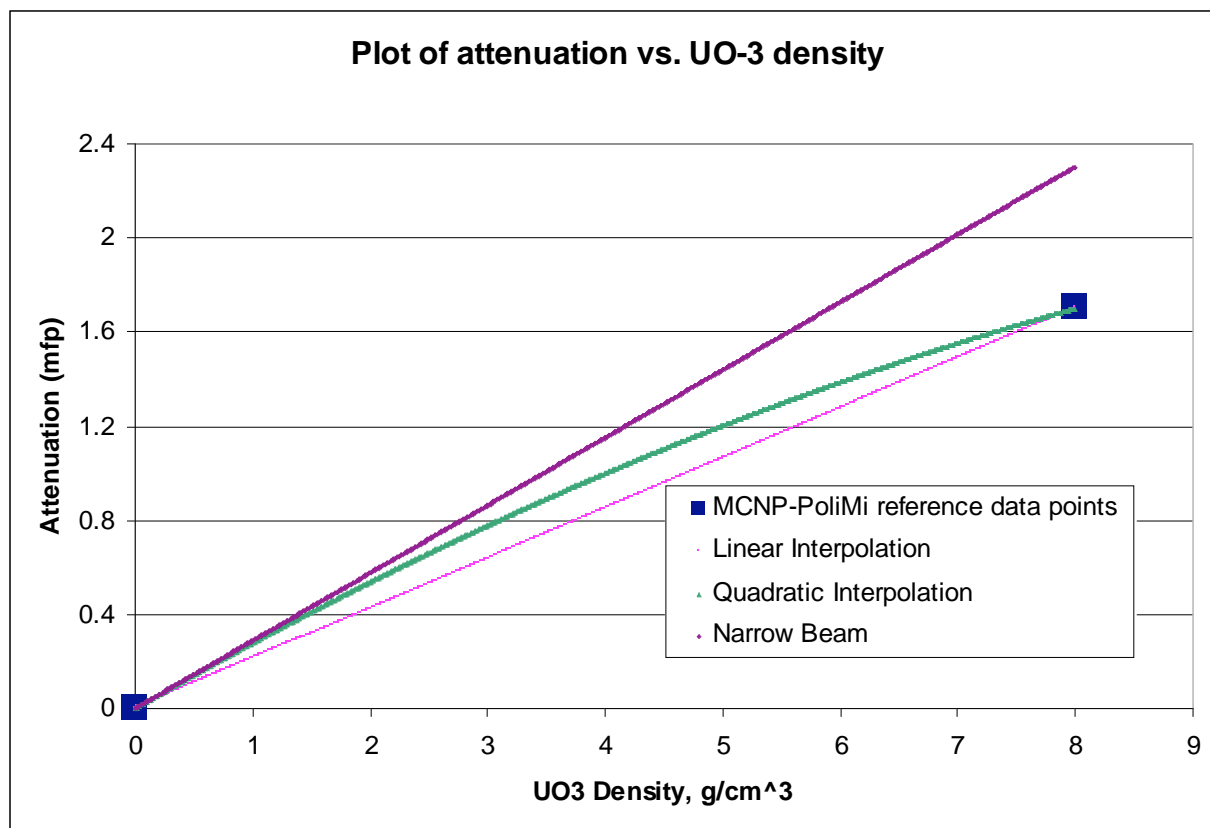
Figure 19   **Plot of Attenuation vs. UO₃ density showing ideal (narrow beam geometry) case, MCNP-PoliMi simulation results, and two different interpolation models**

At a density of 8.00 g/cm³, there is a significant deviation between the attenuation line produced in an ideal geometry and the data point computed by MCNP-PoliMi. This is because the actual geometry differs from the ideal case. Scattered neutrons can appear to be directly transmitted, which causes the effective attenuation to appear lower. The time-correlation methods employed by NMIS reduce, but do not entirely alleviate, this effect. Heavy nuclei, such as uranium isotopes, tend to exacerbate this problem because even neutrons that undergo a significant elastic scattering event will lose only a very small portion of their energy. These neutrons can thus be scattered into one of the detectors in the array and arrive during the fast neutron window, which causes NMIS to underestimate the physical attenuation.

The methodology used in this paper assume that, even though the attenuation values will be different than the ones for an ideal case, that it is possible to linearly interpolate between two measured attenuation values to estimate the unknown density. More than likely, however, this relationship is not linear. In addition to the linear interpolation, Figure 19 also shows a quadratic fit between the two MCNP-PoliMi data points. This curve is one of the infinite number of possible quadratic interpolations between these two data points. If desired, additional reference scans could be conducted in order to more accurately quantify this curve.

Another possible source of error is the assumption presented in Section 4.4, namely that pixel with a given average density will produce the same attenuation value, regardless of the internal geometry of the powder in that pixel. Because two cases produced systematically high results

and another produced systematically low ones, this source of error may be the most significant one. Additional simulations may be able to identify the effects of different pixel geometries on the effective attenuation, which could then be used to refine the algorithm used to estimate the UO_3 mass.

Despite these biases, all of the estimated masses were within 3% of the true mass. This indicates that although there is systemic bias in the results, the effect is small for the three geometries modeled. Two uncertainty analyses indicate that the statistical uncertainty is <0.5% for all simulated measurements. As a result, over the range of measurement times examined, there is no increase in accuracy in the longer measurements. Finally, an analysis of background radiation on the measurements indicates that even in an area with large numbers of background counts, the uncertainty resulting from fluctuations in the background rate will be only half of that due to uncertainty in the number of correlations in the fast neutron peaks for the three model configurations used in this paper.

In measurements with the physical NMIS system, there will be additional sources of error which are not present in the simulations. There will be, for example, uncertainty in detector positions, uncertainty in target position, variations in the temperature of the electronics, and many other factors. While it is unrealistic to assume physical measurements will be able to achieve the same level of accuracy ($\leq 3\%$ in a 4 min scan) as the simulations, the simulation results provide a good starting point which can be used to extrapolate to physical measurements. Based on the results of the nine MCNP-PoliMi simulations, it is expected that an NMIS scan could determine the mass of UO_3 powder within $\pm 10\%$ in one hour or less.

References

1. L. G. Chiang, A. C. Gehl, J. K. Mattingly, J. A. McEvers, J. T. Mihalczo, J. A. Mullens, R. B. Oberer, *Nuclear Materials Identification System Operations Manual,* ORNL/TM-2001/65, Rev. 2, Oak Ridge National Laboratory, August 2001.

2. T. Uckan, M. S. Wyatt, J. T. Mihalczo, T. E. Valentine, J. A. Mullens, T. F. Hannon, *Fissile Deposit Characterization at the Former Oak Ridge K-25 Gaseous Diffusion Plant by* ^{252}*Cf-Source-Driven Measurements*, ORNL/TM-13642, Oak Ridge National Laboratory, May 1998.

3. J. A. Mullens, P. Hausladen, P. R. Bingham, J. T. Mihalczo, "Recent Imaging Measurements with NMIS at ORNL," *Proc. INMM Annual Meeting,* Phoenix, Ariz., July 2005.

4. J. T. Mihalczo, J. A. Mullens, J. K. Mattingly, T. E. Valentine, "Physical Description of Nuclear Materials Identification System (NMIS) Signatures," *Nuclear Instruments and Methods*, **450**, 531–555 (August 2000)

5. T. Gozani, Active Nondestructive Assay of Nuclear Materials: Principles and Applications, Science Applications Inc., California, 1981.

6. "API120 D-T Neutron Generator User Manual", Thermo Electron Corp., Colorado Springs, CO, USA, http://www.thermo.com/eThermo/CMA/PDFs/Various/File_29654.pdf

7. J. T. Mihalczo, P. E. Koehler, T. E. Valentine, L. D. Phillips, *Source Options for Nuclear Weapons Identification System*, ORNL/TM-13025, Oak Ridge National Laboratory, July 1995.

8. G. Knoll, Radiation Detection and Measurement, 3rd Ed., John Wiley & Sons, Massachusetts, 2000.

9. Created by Joel Chesser, Oak Ridge National Laboratory.

10. X-5 Monte Carlo Team, "MCNP – A Monte Carlo N-Particle Transport Code, Version 5," LA-UR-03-1987, Los Alamos National Laboratory, October 2005.

11. M. Marseguerra, E. Padovani, S. A. Pozzi, "Simulating the Wrong Physics Can Generate the Correct Results," *3rd IMACS Seminar on Monte Carlo Methods*, Salzburg, Austria, September 2001.

12. E. Padovani, S. A. Pozzi, *MCNP-PoliMi ver. 1.0 Users Manual*, CESNEF-021125, Library of Nucl. Engr. Dept., Polytechnic of Milan, Italy, November 2002.

13. Personal communication with P. Hausladen, ORNL, February 2007.

Appendix A – MCNP-PoliMi Sample Input Deck

The following input deck is one of the input files used to make a simulated measurement. This
deck corresponds to a vertical height and a single arm angle. A total of 44 input decks were
required for a complete container scan.

```
UO3 Trough Measurement, Rho=8, Minus Side
C Input created on 26-Feb-2006
C Cell Cards
51  1  -8.00 54 -55 (-51:-60) imp:n,p=1 $trough interior
52  12 -7.94 53 -56 (-52:-61) #51 imp:n,p=1 $trough walls
c 53  0         57 -51 imp:n,p=1 $trough interior
108 0        109 -110 111 112 113 114 imp:n,p=1 $ DT emission CCC
114 0 128 -129 130 -131 132 -133 #108 #51 #52
c      #201 #203 #205 #207 #209 #211 #213 #215 #217 #219 #221 #223
c      #225 #227 #229 #231 #233 #235 #237 #239 #241 #243 #245 #247
       #202 #204 #206 #208 #210 #212 #214 #216 #218 #220 #222 #224
       #226 #228 #230 #232 #234 #236 #238 #240 #242 #244 #246 #248
       imp:n,p=1
115  0 -128:129:-130:131:-132:133 imp:n,p=0 $ everything else
202  8  -1.0320 -202 imp:n,p=1 $ detector  1
204  8  -1.0320 -204 imp:n,p=1 $ detector  2
206  8  -1.0320 -206 imp:n,p=1 $ detector  3
208  8  -1.0320 -208 imp:n,p=1 $ detector  4
210  8  -1.0320 -210 imp:n,p=1 $ detector  5
212  8  -1.0320 -212 imp:n,p=1 $ detector  6
214  8  -1.0320 -214 imp:n,p=1 $ detector  7
216  8  -1.0320 -216 imp:n,p=1 $ detector  8
218  8  -1.0320 -218 imp:n,p=1 $ detector  9
220  8  -1.0320 -220 imp:n,p=1 $ detector 10
222  8  -1.0320 -222 imp:n,p=1 $ detector 11
224  8  -1.0320 -224 imp:n,p=1 $ detector 12
226  8  -1.0320 -226 imp:n,p=1 $ detector 13
228  8  -1.0320 -228 imp:n,p=1 $ detector 14
230  8  -1.0320 -230 imp:n,p=1 $ detector 15
232  8  -1.0320 -232 imp:n,p=1 $ detector 16
234  8  -1.0320 -234 imp:n,p=1 $ detector 17
236  8  -1.0320 -236 imp:n,p=1 $ detector 18
238  8  -1.0320 -238 imp:n,p=1 $ detector 19
240  8  -1.0320 -240 imp:n,p=1 $ detector 20
242  8  -1.0320 -242 imp:n,p=1 $ detector 21
244  8  -1.0320 -244 imp:n,p=1 $ detector 22
246  8  -1.0320 -246 imp:n,p=1 $ detector 23
248  8  -1.0320 -248 imp:n,p=1 $ detector 24

C
C Surface Cards
C
51  2 box -6.35   -21.9075 8.3025 12.7   0 0 0 43.815 0 0 0 10.668
52  2 box -7.3025 -22.86   8.3025 14.605 0 0 0 45.72  0 0 0 11.6205
53  2 py -22.86
54  2 py -21.9075
```

```
55   2 py   21.9075
56   2 py   22.86
c 57  2 pz 0.0001
60   2 c/y 0.0 8.3025 6.35
61   2 c/y 0.0 8.3025 7.3025
108 3 sx -56 0.1    $ DT emission surface (sphere)
109 3 sx -56 0.09   $ DT emission surface CCC cell inner
110 3 sx -56 0.11   $ DT emission surface CCC cell outer
111 3 p  0.08749   0  1 -4.89944 $ DT emission top plane, 10 deg arc
112 3 p  0.08749   0 -1 -4.89944 $ DT emission bottom plane
113 3 p  0.41421   1  0 -23.196 $ DT emission right plane, 45 deg arc
114 3 p  0.41421  -1  0 -23.196 $ DT emission left plane
128 px  -56.01   $ problem min x boundary
129 px  150      $ problem max x boundary
130 py  -88.9272 $ problem min y boundary
131 py   88.9272 $ problem max y boundary
132 pz  -50      $ problem min z boundary
133 pz   50      $ problem max z boundary
c 134 k/x -56 0.001 0.001 0.059915 +1 $ effective fan beam
c 135 1 c/z 0 0 15.2165 $ reconstruction circle
202 1 BOX  144.725839  58.241261  -1.270000   0.929042  -2.363997
           0.000000  14.183981   5.574251   0.000000   0.000000   0.000000
           2.540000 $ Angle =   21.454638
204 1 BOX  146.545196  53.498771  -1.270000   0.851588  -2.392989
           0.000000  14.357935   5.109530   0.000000   0.000000   0.000000
           2.540000 $ Angle =   19.589018
206 1 BOX  148.209194  48.699565  -1.270000   0.773232  -2.419445
           0.000000  14.516668   4.639392   0.000000   0.000000   0.000000
           2.540000 $ Angle =   17.723397
208 1 BOX  149.716070  43.848730  -1.270000   0.694056  -2.443335
           0.000000  14.660010   4.164336   0.000000   0.000000   0.000000
           2.540000 $ Angle =   15.857776
210 1 BOX  151.064227  38.951410  -1.270000   0.614144  -2.464635
           0.000000  14.787811   3.684865   0.000000   0.000000   0.000000
           2.540000 $ Angle =   13.992156
212 1 BOX  152.252233  34.012796  -1.270000   0.533581  -2.483323
           0.000000  14.899935   3.201488   0.000000   0.000000   0.000000
           2.540000 $ Angle =   12.126535
214 1 BOX  153.278832  29.038124  -1.270000   0.452453  -2.499377
           0.000000  14.996263   2.714716   0.000000   0.000000   0.000000
           2.540000 $ Angle =   10.260914
216 1 BOX  154.142933  24.032667  -1.270000   0.370844  -2.512782
           0.000000  15.076693   2.225067   0.000000   0.000000   0.000000
           2.540000 $ Angle =    8.395293
218 1 BOX  154.843621  19.001732  -1.270000   0.288843  -2.523523
           0.000000  15.141140   1.733059   0.000000   0.000000   0.000000
           2.540000 $ Angle =    6.529673
220 1 BOX  155.380154  13.950652  -1.270000   0.206536  -2.531589
           0.000000  15.189534   1.239213   0.000000   0.000000   0.000000
           2.540000 $ Angle =    4.664052
222 1 BOX  155.751962   8.884783  -1.270000   0.124009  -2.536971
           0.000000  15.221826   0.744054   0.000000   0.000000   0.000000
           2.540000 $ Angle =    2.798431
224 1 BOX  155.958650   3.809495  -1.270000   0.041351  -2.539663
           0.000000  15.237980   0.248106   0.000000   0.000000   0.000000
           2.540000 $ Angle =    0.932810
226 1 BOX  156.000001  -1.269832  -1.270000  -0.041351  -2.539663
```

```
                0.000000  15.237980  -0.248106   0.000000   0.000000   0.000000
                2.540000 $ Angle =   -0.932810
228 1 BOX  155.875971  -6.347812  -1.270000  -0.124009  -2.536971
                0.000000  15.221826  -0.744054   0.000000   0.000000   0.000000
                2.540000 $ Angle =   -2.798431
230 1 BOX  155.586689 -11.419063  -1.270000  -0.206536  -2.531589
                0.000000  15.189534  -1.239213   0.000000   0.000000   0.000000
                2.540000 $ Angle =   -4.664052
232 1 BOX  155.132465 -16.478208  -1.270000  -0.288843  -2.523523
                0.000000  15.141140  -1.733059   0.000000   0.000000   0.000000
                2.540000 $ Angle =   -6.529673
234 1 BOX  154.513778 -21.519884  -1.270000  -0.370844  -2.512782
                0.000000  15.076693  -2.225067   0.000000   0.000000   0.000000
                2.540000 $ Angle =   -8.395293
236 1 BOX  153.731285 -26.538746  -1.270000  -0.452453  -2.499377
                0.000000  14.996263  -2.714716   0.000000   0.000000   0.000000
                2.540000 $ Angle =  -10.260914
238 1 BOX  152.785815 -31.529473  -1.270000  -0.533581  -2.483323
                0.000000  14.899935  -3.201488   0.000000   0.000000   0.000000
                2.540000 $ Angle =  -12.126535
240 1 BOX  151.678371 -36.486775  -1.270000  -0.614144  -2.464635
                0.000000  14.787811  -3.684865   0.000000   0.000000   0.000000
                2.540000 $ Angle =  -13.992156
242 1 BOX  150.410126 -41.405395  -1.270000  -0.694056  -2.443335
                0.000000  14.660010  -4.164336   0.000000   0.000000   0.000000
                2.540000 $ Angle =  -15.857776
244 1 BOX  148.982426 -46.280120  -1.270000  -0.773232  -2.419445
                0.000000  14.516668  -4.639392   0.000000   0.000000   0.000000
                2.540000 $ Angle =  -17.723397
246 1 BOX  147.396784 -51.105782  -1.270000  -0.851588  -2.392989
                0.000000  14.357935  -5.109530   0.000000   0.000000   0.000000
                2.540000 $ Angle =  -19.589018
248 1 BOX  145.654881 -55.877264  -1.270000  -0.929042  -2.363997
                0.000000  14.183981  -5.574251   0.000000   0.000000   0.000000
                2.540000 $ Angle =  -21.454638


C
C Control Cards and Materials
C
TR1* -56 0 0 -0.466436 -90.466436 90 89.533564 -0.466436 90 -90 -90 0
TR2* 14 0 0 0.000 90.000 90 90.000 0 90 90 90 0 1
TR3* 0 0 0 0.000 90.000 90 90.000 0 90 90 90 0 1
mode n p
m1   NLIB=60C $ HEU
      92235 -0.7753713
      92238 -0.0570187
      8016  -0.16761
m8   NLIB=60C $ organic scintillator
      6000 10
      1001 11
m12  NLIB=60C $ SS-304L
      6000  -0.0003000
      7014  -0.0010000
      14000 -0.0075000
      15031 -0.0004500
      16000 -0.0003000
      24050 -0.0082555
```

```
      24052 -0.1591991
      24053 -0.0180519
      24054 -0.0044935
      25055 -0.0200000
      26054 -0.0397723
      26056 -0.6243401
      26057 -0.0144187
      26058 -0.0019189
      28058 -0.0680770
      28060 -0.0262230
      28061 -0.0011400
      28062 -0.0036340
      28064 -0.0009260
SDEF pos=-56.000000 0.001000 0.001000 ERG=14.100 SUR=108 DIR=1 CCC=108
      EFF=0.0001
PHYS:N J 20.
PHYS:P 0 1 1
CUT:N 25.600000
CUT:P 25.600000 J 0
IDUM 0 1 2 1 J 1 24 202 204 206 208 210 212 214 216 218 220 222 224 226
      228 230 232 234 236 238 240 242 244 246 248
RDUM 0.000150 0.001000
NPS 15100000
DBCN 24886073522007 6J 1 4J 76459
CTME 60000
PRDMP J -60 1
FILES 21 DUMN1 $ 3J 22 DUMN2
```

Appendix B – A Sample Source Detector Time-Correlation file produced by the MCNP-PoliMi Postprocessor

```
 0.0000 0.000000E+00   0.000000E+00   0.000000E+00   0.000000E+00   0.000000E+00   0.000000E+00
 1.0000 0.000000E+00   0.000000E+00   0.000000E+00   0.000000E+00   0.000000E+00   0.000000E+00
 2.0000 0.000000E+00   0.000000E+00   0.000000E+00   0.000000E+00   0.000000E+00   0.000000E+00
 3.0000 0.000000E+00   0.000000E+00   0.000000E+00   0.000000E+00   0.000000E+00   0.000000E+00
 4.0000 0.000000E+00   0.000000E+00   0.000000E+00   0.000000E+00   0.000000E+00   0.000000E+00
 5.0000 0.000000E+00   0.000000E+00   0.000000E+00   0.000000E+00   0.000000E+00   0.000000E+00
 6.0000 0.000000E+00   0.000000E+00   0.000000E+00   0.000000E+00   0.000000E+00   0.000000E+00
 7.0000 0.000000E+00   0.000000E+00   0.000000E+00   0.000000E+00   0.000000E+00   0.000000E+00
 8.0000 0.000000E+00   0.000000E+00   0.000000E+00   0.000000E+00   0.000000E+00   0.000000E+00
 9.0000 0.000000E+00   0.000000E+00   0.000000E+00   0.000000E+00   0.000000E+00   0.000000E+00
10.0000 0.000000E+00   0.000000E+00   0.000000E+00   0.000000E+00   0.000000E+00   0.000000E+00
11.0000 0.000000E+00   0.000000E+00   0.000000E+00   0.000000E+00   0.000000E+00   0.000000E+00
12.0000 0.000000E+00   0.000000E+00   0.000000E+00   0.000000E+00   0.000000E+00   0.000000E+00
13.0000 0.000000E+00   0.000000E+00   0.000000E+00   0.000000E+00   0.000000E+00   0.000000E+00
14.0000 0.000000E+00   0.000000E+00   0.000000E+00   0.000000E+00   0.000000E+00   0.000000E+00
15.0000 0.000000E+00   0.000000E+00   0.000000E+00   0.000000E+00   0.000000E+00   0.000000E+00
16.0000 0.000000E+00   0.000000E+00   0.000000E+00   0.000000E+00   0.000000E+00   0.000000E+00
17.0000 2.133333E-06   0.000000E+00   2.133333E-06   1.666667E-06   4.666667E-07   0.000000E+00
18.0000 2.933333E-06   0.000000E+00   2.933333E-06   2.066667E-06   8.666667E-07   0.000000E+00
19.0000 1.066667E-06   0.000000E+00   1.066667E-06   4.000000E-07   6.666667E-07   0.000000E+00
20.0000 6.000000E-07   0.000000E+00   6.000000E-07   1.333333E-07   4.666667E-07   0.000000E+00
21.0000 6.000000E-07   0.000000E+00   6.000000E-07   1.333333E-07   4.666667E-07   0.000000E+00
22.0000 2.000000E-07   0.000000E+00   2.000000E-07   0.000000E+00   2.000000E-07   0.000000E+00
23.0000 6.666667E-08   0.000000E+00   6.666667E-08   0.000000E+00   6.666667E-08   0.000000E+00
24.0000 1.333333E-07   0.000000E+00   1.333333E-07   0.000000E+00   1.333333E-07   0.000000E+00
25.0000 1.333333E-07   0.000000E+00   1.333333E-07   6.666667E-08   6.666667E-08   0.000000E+00
26.0000 6.666667E-08   0.000000E+00   6.666667E-08   0.000000E+00   6.666667E-08   0.000000E+00
27.0000 2.000000E-07   0.000000E+00   2.000000E-07   0.000000E+00   2.000000E-07   0.000000E+00
28.0000 0.000000E+00   0.000000E+00   0.000000E+00   0.000000E+00   0.000000E+00   0.000000E+00
29.0000 6.666667E-08   0.000000E+00   6.666667E-08   0.000000E+00   6.666667E-08   0.000000E+00
30.0000 7.813334E-05   7.800000E-05   1.333333E-07   7.806667E-05   6.666667E-08   7.793333E-05
31.0000 3.567333E-04   3.556000E-04   1.133333E-06   3.566667E-04   6.666667E-08   3.532667E-04
32.0000 1.824667E-04   1.814667E-04   1.000000E-06   1.824000E-04   6.666667E-08   1.770000E-04
33.0000 9.820000E-05   9.720000E-05   1.000000E-06   9.800000E-05   2.000000E-07   9.060000E-05
34.0000 3.866667E-06   3.600000E-06   2.666667E-07   3.866667E-06   0.000000E+00   0.000000E+00
35.0000 2.266667E-06   2.200000E-06   6.666667E-08   2.200000E-06   6.666667E-08   0.000000E+00
36.0000 1.866667E-06   1.733333E-06   1.333333E-07   1.733333E-06   1.333333E-07   0.000000E+00
37.0000 6.000000E-07   5.333333E-07   6.666667E-08   5.333333E-07   6.666667E-08   0.000000E+00
38.0000 4.666667E-07   4.000000E-07   6.666667E-08   4.000000E-07   6.666667E-08   0.000000E+00
39.0000 4.000000E-07   2.000000E-07   2.000000E-07   2.000000E-07   2.000000E-07   0.000000E+00
40.0000 2.666667E-07   2.666667E-07   0.000000E+00   2.666667E-07   0.000000E+00   0.000000E+00
41.0000 4.000000E-07   4.000000E-07   0.000000E+00   4.000000E-07   0.000000E+00   0.000000E+00
42.0000 3.333333E-07   3.333333E-07   0.000000E+00   2.666667E-07   6.666667E-08   0.000000E+00
43.0000 4.000000E-07   4.000000E-07   0.000000E+00   3.333333E-07   6.666667E-08   0.000000E+00
44.0000 1.333333E-07   1.333333E-07   0.000000E+00   1.333333E-07   0.000000E+00   0.000000E+00
45.0000 2.000000E-07   6.666667E-08   1.333333E-07   1.333333E-07   6.666667E-08   0.000000E+00
46.0000 2.666667E-07   2.000000E-07   6.666667E-08   2.000000E-07   6.666667E-08   0.000000E+00
47.0000 2.666667E-07   2.000000E-07   6.666667E-08   1.333333E-07   1.333333E-07   0.000000E+00
48.0000 4.000000E-07   3.333333E-07   6.666667E-08   2.000000E-07   2.000000E-07   0.000000E+00
49.0000 2.000000E-07   2.000000E-07   0.000000E+00   2.000000E-07   0.000000E+00   0.000000E+00
50.0000 2.000000E-07   2.000000E-07   0.000000E+00   2.000000E-07   0.000000E+00   0.000000E+00
51.0000 1.333333E-07   1.333333E-07   0.000000E+00   6.666667E-08   6.666667E-08   0.000000E+00
52.0000 1.333333E-07   1.333333E-07   0.000000E+00   6.666667E-08   6.666667E-08   0.000000E+00
53.0000 6.000000E-07   3.333333E-07   2.666667E-07   6.666667E-08   5.333333E-07   0.000000E+00
54.0000 5.333333E-07   4.666667E-07   6.666667E-08   6.666667E-08   4.666667E-07   0.000000E+00
55.0000 2.000000E-07   1.333333E-07   6.666667E-08   6.666667E-08   1.333333E-07   0.000000E+00
56.0000 2.000000E-07   2.000000E-07   0.000000E+00   1.333333E-07   6.666667E-08   0.000000E+00
57.0000 1.333333E-07   1.333333E-07   0.000000E+00   1.333333E-07   0.000000E+00   0.000000E+00
58.0000 2.000000E-07   2.000000E-07   0.000000E+00   1.333333E-07   6.666667E-08   0.000000E+00
59.0000 6.666667E-08   6.666667E-08   0.000000E+00   6.666667E-08   0.000000E+00   0.000000E+00
60.0000 3.333333E-07   2.000000E-07   1.333333E-07   6.666667E-08   2.666667E-07   0.000000E+00
61.0000 4.000000E-07   3.333333E-07   6.666667E-08   6.666667E-08   3.333333E-07   0.000000E+00
62.0000 2.666667E-07   2.000000E-07   6.666667E-08   2.666667E-07   0.000000E+00   0.000000E+00
63.0000 2.000000E-07   1.333333E-07   6.666667E-08   6.666667E-08   1.333333E-07   0.000000E+00
64.0000 2.666667E-07   2.666667E-07   0.000000E+00   6.666667E-08   2.000000E-07   0.000000E+00
```

```
 65.0000 2.666667E-07  2.666667E-07  0.000000E+00  1.333333E-07  1.333333E-07  0.000000E+00
 66.0000 2.666667E-07  2.666667E-07  0.000000E+00  0.000000E+00  2.666667E-07  0.000000E+00
 67.0000 1.333333E-07  1.333333E-07  0.000000E+00  6.666667E-08  6.666667E-08  0.000000E+00
 68.0000 2.666667E-07  2.666667E-07  0.000000E+00  6.666667E-08  2.000000E-07  0.000000E+00
 69.0000 4.000000E-07  3.333333E-07  6.666667E-08  1.333333E-07  2.666667E-07  0.000000E+00
 70.0000 2.666667E-07  2.000000E-07  6.666667E-08  0.000000E+00  2.666667E-07  0.000000E+00
 71.0000 1.333333E-07  1.333333E-07  0.000000E+00  1.333333E-07  0.000000E+00  0.000000E+00
 72.0000 2.666667E-07  2.666667E-07  0.000000E+00  1.333333E-07  1.333333E-07  0.000000E+00
 73.0000 0.000000E+00  0.000000E+00  0.000000E+00  0.000000E+00  0.000000E+00  0.000000E+00
 74.0000 2.000000E-07  2.000000E-07  0.000000E+00  6.666667E-08  1.333333E-07  0.000000E+00
 75.0000 2.666667E-07  2.666667E-07  0.000000E+00  0.000000E+00  2.666667E-07  0.000000E+00
 76.0000 1.333333E-07  1.333333E-07  0.000000E+00  0.000000E+00  1.333333E-07  0.000000E+00
 77.0000 1.333333E-07  1.333333E-07  0.000000E+00  0.000000E+00  1.333333E-07  0.000000E+00
 78.0000 1.333333E-07  1.333333E-07  0.000000E+00  6.666667E-08  6.666667E-08  0.000000E+00
 79.0000 2.000000E-07  2.000000E-07  0.000000E+00  0.000000E+00  2.000000E-07  0.000000E+00
 80.0000 1.333333E-07  1.333333E-07  0.000000E+00  6.666667E-08  6.666667E-08  0.000000E+00
 81.0000 1.333333E-07  6.666667E-08  6.666667E-08  0.000000E+00  1.333333E-07  0.000000E+00
 82.0000 1.333333E-07  1.333333E-07  0.000000E+00  0.000000E+00  1.333333E-07  0.000000E+00
 83.0000 0.000000E+00  0.000000E+00  0.000000E+00  0.000000E+00  0.000000E+00  0.000000E+00
 84.0000 6.666667E-08  6.666667E-08  0.000000E+00  0.000000E+00  6.666667E-08  0.000000E+00
 85.0000 2.000000E-07  2.000000E-07  0.000000E+00  6.666667E-08  1.333333E-07  0.000000E+00
 86.0000 6.666667E-08  6.666667E-08  0.000000E+00  0.000000E+00  6.666667E-08  0.000000E+00
 87.0000 2.666667E-07  2.666667E-07  0.000000E+00  6.666667E-08  2.000000E-07  0.000000E+00
 88.0000 0.000000E+00  0.000000E+00  0.000000E+00  0.000000E+00  0.000000E+00  0.000000E+00
 89.0000 6.666667E-08  0.000000E+00  6.666667E-08  0.000000E+00  6.666667E-08  0.000000E+00
 90.0000 6.666667E-08  0.000000E+00  6.666667E-08  0.000000E+00  6.666667E-08  0.000000E+00
 91.0000 6.666667E-08  0.000000E+00  6.666667E-08  0.000000E+00  6.666667E-08  0.000000E+00
 92.0000 0.000000E+00  0.000000E+00  0.000000E+00  0.000000E+00  0.000000E+00  0.000000E+00
 93.0000 0.000000E+00  0.000000E+00  0.000000E+00  0.000000E+00  0.000000E+00  0.000000E+00
 94.0000 0.000000E+00  0.000000E+00  0.000000E+00  0.000000E+00  0.000000E+00  0.000000E+00
 95.0000 6.666667E-08  6.666667E-08  0.000000E+00  0.000000E+00  6.666667E-08  0.000000E+00
 96.0000 1.333333E-07  6.666667E-08  6.666667E-08  0.000000E+00  1.333333E-07  0.000000E+00
 97.0000 1.333333E-07  6.666667E-08  6.666667E-08  0.000000E+00  1.333333E-07  0.000000E+00
 98.0000 0.000000E+00  0.000000E+00  0.000000E+00  0.000000E+00  0.000000E+00  0.000000E+00
 99.0000 0.000000E+00  0.000000E+00  0.000000E+00  0.000000E+00  0.000000E+00  0.000000E+00
100.0000 6.666667E-08  6.666667E-08  0.000000E+00  0.000000E+00  6.666667E-08  0.000000E+00
101.0000 0.000000E+00  0.000000E+00  0.000000E+00  0.000000E+00  0.000000E+00  0.000000E+00
102.0000 6.666667E-08  6.666667E-08  0.000000E+00  0.000000E+00  6.666667E-08  0.000000E+00
103.0000 0.000000E+00  0.000000E+00  0.000000E+00  0.000000E+00  0.000000E+00  0.000000E+00
104.0000 6.666667E-08  6.666667E-08  0.000000E+00  0.000000E+00  6.666667E-08  0.000000E+00
105.0000 1.333333E-07  1.333333E-07  0.000000E+00  0.000000E+00  1.333333E-07  0.000000E+00
106.0000 0.000000E+00  0.000000E+00  0.000000E+00  0.000000E+00  0.000000E+00  0.000000E+00
107.0000 0.000000E+00  0.000000E+00  0.000000E+00  0.000000E+00  0.000000E+00  0.000000E+00
108.0000 0.000000E+00  0.000000E+00  0.000000E+00  0.000000E+00  0.000000E+00  0.000000E+00
109.0000 0.000000E+00  0.000000E+00  0.000000E+00  0.000000E+00  0.000000E+00  0.000000E+00
110.0000 6.666667E-08  6.666667E-08  0.000000E+00  0.000000E+00  6.666667E-08  0.000000E+00
111.0000 0.000000E+00  0.000000E+00  0.000000E+00  0.000000E+00  0.000000E+00  0.000000E+00
112.0000 0.000000E+00  0.000000E+00  0.000000E+00  0.000000E+00  0.000000E+00  0.000000E+00
113.0000 6.666667E-08  6.666667E-08  0.000000E+00  0.000000E+00  6.666667E-08  0.000000E+00
114.0000 0.000000E+00  0.000000E+00  0.000000E+00  0.000000E+00  0.000000E+00  0.000000E+00
115.0000 1.333333E-07  1.333333E-07  0.000000E+00  0.000000E+00  1.333333E-07  0.000000E+00
116.0000 0.000000E+00  0.000000E+00  0.000000E+00  0.000000E+00  0.000000E+00  0.000000E+00
117.0000 0.000000E+00  0.000000E+00  0.000000E+00  0.000000E+00  0.000000E+00  0.000000E+00
118.0000 6.666667E-08  6.666667E-08  0.000000E+00  0.000000E+00  6.666667E-08  0.000000E+00
119.0000 0.000000E+00  0.000000E+00  0.000000E+00  0.000000E+00  0.000000E+00  0.000000E+00
120.0000 2.000000E-07  2.000000E-07  0.000000E+00  0.000000E+00  2.000000E-07  0.000000E+00
121.0000 0.000000E+00  0.000000E+00  0.000000E+00  0.000000E+00  0.000000E+00  0.000000E+00
122.0000 1.333333E-07  1.333333E-07  0.000000E+00  0.000000E+00  1.333333E-07  0.000000E+00
123.0000 0.000000E+00  0.000000E+00  0.000000E+00  0.000000E+00  0.000000E+00  0.000000E+00
124.0000 0.000000E+00  0.000000E+00  0.000000E+00  0.000000E+00  0.000000E+00  0.000000E+00
125.0000 0.000000E+00  0.000000E+00  0.000000E+00  0.000000E+00  0.000000E+00  0.000000E+00
126.0000 0.000000E+00  0.000000E+00  0.000000E+00  0.000000E+00  0.000000E+00  0.000000E+00
127.0000 0.000000E+00  0.000000E+00  0.000000E+00  0.000000E+00  0.000000E+00  0.000000E+00
128.0000 0.000000E+00  0.000000E+00  0.000000E+00  0.000000E+00  0.000000E+00  0.000000E+00
129.0000 0.000000E+00  0.000000E+00  0.000000E+00  0.000000E+00  0.000000E+00  0.000000E+00
130.0000 0.000000E+00  0.000000E+00  0.000000E+00  0.000000E+00  0.000000E+00  0.000000E+00
131.0000 6.666667E-08  6.666667E-08  0.000000E+00  0.000000E+00  6.666667E-08  0.000000E+00
132.0000 0.000000E+00  0.000000E+00  0.000000E+00  0.000000E+00  0.000000E+00  0.000000E+00
133.0000 6.666667E-08  6.666667E-08  0.000000E+00  0.000000E+00  6.666667E-08  0.000000E+00
134.0000 0.000000E+00  0.000000E+00  0.000000E+00  0.000000E+00  0.000000E+00  0.000000E+00
135.0000 6.666667E-08  6.666667E-08  0.000000E+00  0.000000E+00  6.666667E-08  0.000000E+00
```

```
136.0000 0.000000E+00   0.000000E+00   0.000000E+00   0.000000E+00   0.000000E+00   0.000000E+00
137.0000 0.000000E+00   0.000000E+00   0.000000E+00   0.000000E+00   0.000000E+00   0.000000E+00
138.0000 0.000000E+00   0.000000E+00   0.000000E+00   0.000000E+00   0.000000E+00   0.000000E+00
139.0000 6.666667E-08   6.666667E-08   0.000000E+00   0.000000E+00   6.666667E-08   0.000000E+00
140.0000 0.000000E+00   0.000000E+00   0.000000E+00   0.000000E+00   0.000000E+00   0.000000E+00
141.0000 0.000000E+00   0.000000E+00   0.000000E+00   0.000000E+00   0.000000E+00   0.000000E+00
142.0000 0.000000E+00   0.000000E+00   0.000000E+00   0.000000E+00   0.000000E+00   0.000000E+00
143.0000 0.000000E+00   0.000000E+00   0.000000E+00   0.000000E+00   0.000000E+00   0.000000E+00
144.0000 0.000000E+00   0.000000E+00   0.000000E+00   0.000000E+00   0.000000E+00   0.000000E+00
145.0000 0.000000E+00   0.000000E+00   0.000000E+00   0.000000E+00   0.000000E+00   0.000000E+00
146.0000 0.000000E+00   0.000000E+00   0.000000E+00   0.000000E+00   0.000000E+00   0.000000E+00
147.0000 0.000000E+00   0.000000E+00   0.000000E+00   0.000000E+00   0.000000E+00   0.000000E+00
148.0000 0.000000E+00   0.000000E+00   0.000000E+00   0.000000E+00   0.000000E+00   0.000000E+00
149.0000 6.666667E-08   6.666667E-08   0.000000E+00   0.000000E+00   6.666667E-08   0.000000E+00
150.0000 0.000000E+00   0.000000E+00   0.000000E+00   0.000000E+00   0.000000E+00   0.000000E+00
151.0000 6.666667E-08   6.666667E-08   0.000000E+00   0.000000E+00   6.666667E-08   0.000000E+00
152.0000 0.000000E+00   0.000000E+00   0.000000E+00   0.000000E+00   0.000000E+00   0.000000E+00
153.0000 6.666667E-08   0.000000E+00   6.666667E-08   0.000000E+00   6.666667E-08   0.000000E+00
154.0000 0.000000E+00   0.000000E+00   0.000000E+00   0.000000E+00   0.000000E+00   0.000000E+00
155.0000 0.000000E+00   0.000000E+00   0.000000E+00   0.000000E+00   0.000000E+00   0.000000E+00
156.0000 6.666667E-08   6.666667E-08   0.000000E+00   0.000000E+00   6.666667E-08   0.000000E+00
157.0000 0.000000E+00   0.000000E+00   0.000000E+00   0.000000E+00   0.000000E+00   0.000000E+00
158.0000 0.000000E+00   0.000000E+00   0.000000E+00   0.000000E+00   0.000000E+00   0.000000E+00
159.0000 6.666667E-08   6.666667E-08   0.000000E+00   0.000000E+00   6.666667E-08   0.000000E+00
160.0000 0.000000E+00   0.000000E+00   0.000000E+00   0.000000E+00   0.000000E+00   0.000000E+00
161.0000 0.000000E+00   0.000000E+00   0.000000E+00   0.000000E+00   0.000000E+00   0.000000E+00
162.0000 0.000000E+00   0.000000E+00   0.000000E+00   0.000000E+00   0.000000E+00   0.000000E+00
163.0000 0.000000E+00   0.000000E+00   0.000000E+00   0.000000E+00   0.000000E+00   0.000000E+00
164.0000 0.000000E+00   0.000000E+00   0.000000E+00   0.000000E+00   0.000000E+00   0.000000E+00
165.0000 6.666667E-08   6.666667E-08   0.000000E+00   0.000000E+00   6.666667E-08   0.000000E+00
166.0000 0.000000E+00   0.000000E+00   0.000000E+00   0.000000E+00   0.000000E+00   0.000000E+00
167.0000 0.000000E+00   0.000000E+00   0.000000E+00   0.000000E+00   0.000000E+00   0.000000E+00
168.0000 0.000000E+00   0.000000E+00   0.000000E+00   0.000000E+00   0.000000E+00   0.000000E+00
169.0000 0.000000E+00   0.000000E+00   0.000000E+00   0.000000E+00   0.000000E+00   0.000000E+00
170.0000 0.000000E+00   0.000000E+00   0.000000E+00   0.000000E+00   0.000000E+00   0.000000E+00
171.0000 0.000000E+00   0.000000E+00   0.000000E+00   0.000000E+00   0.000000E+00   0.000000E+00
172.0000 0.000000E+00   0.000000E+00   0.000000E+00   0.000000E+00   0.000000E+00   0.000000E+00
173.0000 0.000000E+00   0.000000E+00   0.000000E+00   0.000000E+00   0.000000E+00   0.000000E+00
174.0000 0.000000E+00   0.000000E+00   0.000000E+00   0.000000E+00   0.000000E+00   0.000000E+00
175.0000 0.000000E+00   0.000000E+00   0.000000E+00   0.000000E+00   0.000000E+00   0.000000E+00
176.0000 0.000000E+00   0.000000E+00   0.000000E+00   0.000000E+00   0.000000E+00   0.000000E+00
177.0000 0.000000E+00   0.000000E+00   0.000000E+00   0.000000E+00   0.000000E+00   0.000000E+00
178.0000 0.000000E+00   0.000000E+00   0.000000E+00   0.000000E+00   0.000000E+00   0.000000E+00
179.0000 0.000000E+00   0.000000E+00   0.000000E+00   0.000000E+00   0.000000E+00   0.000000E+00
180.0000 0.000000E+00   0.000000E+00   0.000000E+00   0.000000E+00   0.000000E+00   0.000000E+00
181.0000 0.000000E+00   0.000000E+00   0.000000E+00   0.000000E+00   0.000000E+00   0.000000E+00
182.0000 0.000000E+00   0.000000E+00   0.000000E+00   0.000000E+00   0.000000E+00   0.000000E+00
183.0000 0.000000E+00   0.000000E+00   0.000000E+00   0.000000E+00   0.000000E+00   0.000000E+00
184.0000 0.000000E+00   0.000000E+00   0.000000E+00   0.000000E+00   0.000000E+00   0.000000E+00
185.0000 0.000000E+00   0.000000E+00   0.000000E+00   0.000000E+00   0.000000E+00   0.000000E+00
186.0000 6.666667E-08   0.000000E+00   6.666667E-08   0.000000E+00   6.666667E-08   0.000000E+00
187.0000 0.000000E+00   0.000000E+00   0.000000E+00   0.000000E+00   0.000000E+00   0.000000E+00
188.0000 0.000000E+00   0.000000E+00   0.000000E+00   0.000000E+00   0.000000E+00   0.000000E+00
189.0000 0.000000E+00   0.000000E+00   0.000000E+00   0.000000E+00   0.000000E+00   0.000000E+00
190.0000 0.000000E+00   0.000000E+00   0.000000E+00   0.000000E+00   0.000000E+00   0.000000E+00
191.0000 0.000000E+00   0.000000E+00   0.000000E+00   0.000000E+00   0.000000E+00   0.000000E+00
192.0000 0.000000E+00   0.000000E+00   0.000000E+00   0.000000E+00   0.000000E+00   0.000000E+00
193.0000 6.666667E-08   6.666667E-08   0.000000E+00   0.000000E+00   6.666667E-08   0.000000E+00
194.0000 0.000000E+00   0.000000E+00   0.000000E+00   0.000000E+00   0.000000E+00   0.000000E+00
195.0000 0.000000E+00   0.000000E+00   0.000000E+00   0.000000E+00   0.000000E+00   0.000000E+00
196.0000 0.000000E+00   0.000000E+00   0.000000E+00   0.000000E+00   0.000000E+00   0.000000E+00
197.0000 0.000000E+00   0.000000E+00   0.000000E+00   0.000000E+00   0.000000E+00   0.000000E+00
198.0000 0.000000E+00   0.000000E+00   0.000000E+00   0.000000E+00   0.000000E+00   0.000000E+00
199.0000 6.666667E-08   0.000000E+00   6.666667E-08   0.000000E+00   6.666667E-08   0.000000E+00
200.0000 0.000000E+00   0.000000E+00   0.000000E+00   0.000000E+00   0.000000E+00   0.000000E+00
```

Appendix C – MCNP-PoliMi input cards used to define the container geometry for the three test cases.

Case 1

```
UO3 Trough Measurement, Case1c, Minus Side
C Input created on 26-Feb-2006
C Cell Cards
51  1  -8.00 54 -55 -57 (-51:-60) imp:n,p=1 $trough interior
52  12 -7.94 53 -56 (-52:-61) #51 #53 imp:n,p=1 $trough walls
53  1  -7.00           57 -51 imp:n,p=1 $trough interior


C
C Surface Cards
C
51  2 box -6.35   -21.9075 8.3025 12.7   0 0 0 43.815 0 0 0 10.668
52  2 box -7.3025 -22.86   8.3025 14.605 0 0 0 45.72  0 0 0 11.6205
53  2 py -22.86
54  2 py -21.9075
55  2 py  21.9075
56  2 py  22.86
57  2 pz 11.9999
60  2 c/y 0.0 8.3025 6.35
61  2 c/y 0.0 8.3025 7.3025


C
C Control Cards and Materials
C
TR2* 14 0 0 0.000 90.000 90 90.000 0 90 90 90 0 1
```

Case 2

```
UO3 Trough Measurement, Case 2c, Minus Side
C Input created on 26-Feb-2006
C Cell Cards
51  1  -8.00 54 -55 57 (-51:-60)  imp:n,p=1 $trough interior
52  12 -7.94 53 -56 (-52:-61) #51 #53 imp:n,p=1 $trough walls
53  0           -57 -51 imp:n,p=1 $trough interior


C
C Surface Cards
C
51  2 box -6.35   -21.9075 8.3025 12.7   0 0 0 43.815 0 0 0 10.668
52  2 box -7.3025 -22.86   8.3025 14.605 0 0 0 45.72  0 0 0 11.6205
53  2 py -22.86
54  2 py -21.9075
55  2 py  21.9075
56  2 py  22.86
57  2 p 0.55118 0 -1 -13.5
60  2 c/y 0.0 8.3025 6.35
61  2 c/y 0.0 8.3025 7.3025


C
C Control Cards and Materials
C
TR1* -56 0 0 -0.466436 -90.466436 90 89.533564 -0.466436 90 -90 -90 0
```

```
TR2* 14 0 0 0.000 90.000 90 90.000 0 90 90 90 0 1
TR3* 0 0 0 0.000 90.000 90 90.000 0 90 90 90 0 1
```

Case 3

```
UO3 Trough Measurement, Case 3c, Minus Side
C Input created on 26-Feb-2006
C Cell Cards
51  1  -8.00 54 -55 58 (-51:-60)  imp:n,p=1 $trough interior
52  12 -7.94 53 -56 (-52:-61) #51 #58 imp:n,p=1 $trough walls
58  0          -58        imp:n,p=1

C
C Surface Cards
C
51  2 box -6.35   -21.9075 8.3025 12.7   0 0 0 43.815 0 0 0 10.668
52  2 box -7.3025 -22.86   8.3025 14.605 0 0 0 45.72  0 0 0 11.6205
53  2 py -22.86
54  2 py -21.9075
55  2 py  21.9075
56  2 py  22.86
58  2 sz 12 5
60  2 c/y 0.0 8.3025 6.35
61  2 c/y 0.0 8.3025 7.3025

C
C Control Cards and Materials
C
TR1* -56 0 0 -0.466436 -90.466436 90 89.533564 -0.466436 90 -90 -90 0
TR2* 14 0 0 0.000 90.000 90 90.000 0 90 90 90 0 1
TR3* 0 0 0 0.000 90.000 90 90.000 0 90 90 90 0 1
```